Influence of a discontinuity on the spectral and fractal analysis of one-dimensional data

R. P. H. Berton

Nonlinear Processes in Geophysics (2004) 11: 659–682
SRef-ID: 1607-7946/npg/2004-11-659

Nonlinear Processes in Geophysics

Influence of a discontinuity on the spectral and fractal analysis of one-dimensional data

R. P. H. Berton

ONERA, Chemin de la Hunière, F-91761 Palaiseau Cedex, France

Received: 11 February 2004 – Revised: 6 September 2004 – Accepted: 8 September 2004 – Published: 15 December 2004

Abstract. The analysis of a data area or segment containing steep transitions between regions with different textures (for example a cloud and its background) leads to addressing the problem of discontinuities and their impact on texture analysis. In that purpose, an original one-dimensional analytical model of spectrum and roughness function has been worked out, with a discontinuity between two fractal regions, each one specified by its average μ, standard deviation σ, spectral index β and Hurst exponent H. This has the advantage of not needing the generation of a fractal structure with a particular algorithm or random functions and clearly puts into evidence the role played by the average in generating spectral poles and side lobes.

After validation of the model calibration, a parametric study is carried out in order to understand the influence of this discontinuity on the estimation of the spectral index β and the Hurst parameter H. It shows that for a pure μ-gap, H is well estimated everywhere, though overestimated, and β is overestimated in the anti-correlation range and saturates in the correlation range. For a pure σ-gap the retrieval of H is excellent everywhere and the behaviour of β is better than for a μ-gap, leading to less overestimation in the anti-correlation range. For a pure β-gap, saturation degrades measurements in the case of raw data and the medium with smaller spectral index is predominant in the case of trend-corrected data. For a pure H-gap, there is also dominance of the medium with smaller fractal exponent.

1 Introduction

The necessity of working out realistic models for the generation of natural scenes including clouds or sea waves is not to be demonstrated. The scope of such models is to provide either the spatial distribution of physical characteristics in the medium (elevation, temperature, water content) in one, two or even three dimensions, or directly a two-dimensional image (radiance). Moreover, such a generator should satisfy the constraint of not consuming too much computer time.

The most common algorithm to perform this task is based on the Fourier transform (Lévesque, 1991; Simoneau et al., 2002) implemented as a fast Fourier transform (FFT). Given the slope $-\beta$ (in logarithmic scales) and the outer scale wave number k_0, the Power-Spectral Density (PSD) is defined generally in two dimensions as:

$$P(u, v) = P_0 \left(k_0^2 + u^2 + v^2\right)^{-\beta/2}. \quad (1)$$

A map of fluctuations $F(x, y)$ is then built up from the amplitude, $\sqrt{P(u, v)}$, and a set of random phases $\Phi(u, v)$ by inverse Fourier transform:

$$F(x, y) = \iint_D \sqrt{P(u, v)} e^{i\Phi(u,v)} e^{-i(ux+vy)} du dv \quad (2)$$

or in practice by discrete Fourier transform (DFT):

$$F(x, y) = \sum_{m=1}^{M} \sum_{n=1}^{N} \sqrt{P(m\Delta u, n\Delta v)} e^{i\Phi_{mn}} e^{-i(mx\Delta u + ny\Delta v)}. \quad (3)$$

The corresponding relations in one dimension are obtained by simply removing the variable v in the above expressions (1), (2) and (3).

Conversely, the parameters β and k_0 can be rather easily retrieved from original data by classical spectral analysis in one (Davis et al., 1996) or two dimensions (Moghaddam et al., 1991; Tessendorf et al., 1992).

In the context of developed turbulence, multiplicative cascades provide another method widely used to build a fractal random process (Cahalan, 1994; Davis et al., 1994; Menabde, 1998). Another algorithm which has gained much popularity is based on Weierstrass-Mandelbrot series and is known as simulating at best a fractional Brownian motion FBM (Berry and Lewis, 1980; Ausloos and Berman, 1985; Saupe, 1988; Cianciolo, 1993; Chen et al., 1996; Jennane et al., 1997; Berizzi et al.,1997; Bachelier et al., 1998).

Correspondence to: R. P. H. Berton
(berton@onera.fr)

Given the so-called roughness and lacunarity parameters H ($0 \leq H \leq 1$) and γ ($1<\gamma$), and a set of random phases Φ_m uniformly distributed, the one dimensional function can be written (Berry and Lewis, 1980):

$$W_{1D}(x) = \sum_{m=-\infty}^{+\infty} \gamma^{-mH} \left(1 - e^{i\gamma^m k_0 x}\right) e^{i\Phi_m}. \quad (4)$$

It is also possible to define the series with real sine functions (Saupe, 1988):

$$W_{1D}(x) = \sum_{m=-\infty}^{+\infty} \gamma^{-mH} \sin\left(\gamma^m k_0 x + \Phi_m\right). \quad (4bis)$$

It can be proved that H is the true roughness parameter (Berry and Lewis, 1980; Hunt, 1998). The ordinary Brownian motion is obtained for $H = 1/2$, and corresponds to non-correlated fluctuations, whereas the sub-ranges $0 \leq H < 1/2$ and $1/2 < H \leq 1$ correspond respectively to anti-correlated and correlated fluctuations, or anti-persistence and persistence.

In two dimensions a map of fractal fluctuations $W_{2D}(x, y)$ can be obtained from two independent sets of random phases Φ_{mn} and Ψ_{mn} by the sums (Jennane et al., 1997):

$$W_{2D}(x, y) = \sum_{m=-\infty}^{+\infty} \sum_{n=-\infty}^{+\infty} \gamma^{\frac{m+n}{2}} \frac{\left[1 - e^{ik_0(\gamma^m x + \gamma^n y)}\right] e^{i\Phi_{mn}} + \left[1 - e^{ik_0(-\gamma^m x + \gamma^n y)}\right] e^{i\Psi_{mn}}}{\left[\gamma^{2m} + \gamma^{2n}\right]^{\frac{H+1}{2}}} \quad (5)$$

but this is not the unique possibility, and Eq. (4bis) can be also generalised as (Saupe, 1988):

$$W_{1D}(x) = \sum_{m=-\infty}^{+\infty} \sum_{n=-\infty}^{+\infty} \gamma^{-(m+n)H} \sin\left(\gamma^m k_0 x + \Phi_m\right) \sin\left(\gamma^n k_0 Y + \Psi_n\right). \quad (5bis)$$

The roughness parameter H, or Hurst exponent, at least can be retrieved by various methods, including the rescaled-range analysis (Hurst, 1951), the perimeter-area relation (Lovejoy, 1982; Gotoh and Fujii, 1998), the box-counting method (Theiler, 1990; Malinowski and Zawadzki, 1993; Buczkowski et al., 1998; Carvalho and Silva Dias, 1998), the detrended fluctuation analysis or DFA (Ivanova and Ausloos, 1999; Chen et al., 2002), variograms (Curran, 1988; Germann and Joss, 2001) and wavelet transforms (Simonsen et al., 1998). DFA and spectral analysis have been shown to provide the same information (Heneghan and McDarby, 2000). These methods work well only for Gaussian processes, and poorly for non-Gaussian processes (Malamud and Turcotte, 1999). Certain authors (Scafetta et al., 2001; Scafetta and Grigolini, 2002) proposed a new method, the diffusion entropy analysis (DEA) which is also efficient for non-Gaussian processes, such as Levy flights.

Yet another way of fractal synthesis consists in integrating a Gaussian white noise by means of Riemann-Liouville integral (Mandelbrot and Van Ness, 1968). This method explained in App. A3 will be used here to confirm the calibration of our analytical spectrum and fractal function.

The spectral and fractal approaches are related to some extent, because, under conditions of homogeneity and through application of the Wiener-Khinchine theorem, the following relation holds for a FBM (Moghaddam et al., 1991; Mallat, 1998; van den Heuvel et al., 2000):

$$\beta = 2H + E, \quad (6)$$

where E is the topological dimension of the embedding space (E = 1 for a line, E = 2 for a plane). In one dimension, the spectral index β of a FBM is therefore such that $1 \leq \beta \leq 3$. The non-correlated ordinary Brownian motion is obtained for β = 2 and anticorrelation and correlation subranges are respectively such that $1 \leq \beta < 2$ and $2 < \beta \leq 3$. We shall examine the relevance of relation (6) in Sect. 4.

Reciprocally, by derivation of a FBM, a fractional Gaussian noise FGN is obtained, and relation (6) writes in this case (Heneghan and McDarby, 2000):

$$\beta = 2H - E, \quad (7)$$

In one dimension, the spectral index β of a FGN is therefore such that $-1 \leq \beta \leq 1$ and the non-correlated white noise is obtained for β = 0.

Much work has been devoted to the spatial analysis of clouds, namely cumulus (Malinowski and Zawadzki, 1993; Gotoh and Fujii, 1998), stratocumulus (Davis et al., 1996; Ivanova et al., 1999), cirrus (van den Heuvel et al., 2000; Ivanova et al., 2003), stratus (Ivanova and Ausloos, 1999; Ivanova et al., 2002), mixed mesoscale clouds (Carvalho and Silva Dias, 1998) or landscape data (De Cola, 1989; Southgate and Möller, 2000). Typical values found by these authors in clouds are in the range 1.1–1.7 for one-dimensional spectral indices β (Davis et al., 1996; van den Heuvel et al., 2000) and in the range 0.2–0.6 for Hurst exponents H (Malinowski and Zawadzki, 1993; Gotoh and Fujii, 1998; Ivanova and Ackerman, 1999; Ivanova and Ausloos, 1999; van den Heuvel et al., 2000). Attempts have been made to relate the fractal texture of the medium with the spectral structure of resulting images under simplifying assumptions about the illumination (Kube and Pentland, 1988).

Actually, the quality of the finally synthesised data depends on how accurately the relevant parameters β, k_0, H or γ are retrieved from natural data. In particular, the inhomogeneity of data can lead to large variations (Ivanova and Ausloos, 1999; Ivanova et al., 1999). The aim of our paper is to model the parameters β and H of one-dimensional measurements performed along the trajectory of the instrument carrier (aircraft, balloon, rocket) and to show how a discontinuity between two homogeneous regions can modify the estimation of β and H.

The original point is that no random noise generator is used in our model, so only the intrinsic spectral or fractal properties of the media are taken into account, and their statistical distributions need not be specified. Generally, works

devoted to the estimation of statistical parameters (Taqqu et al., 1995; Schmittbuhl et al., 1995; Rangarajan and Ding, 2000; Chen et al., 2002) deal with signals generated by Fourier filtering method (FFM) of a Gaussian noise and mix up the statistical properties of the random number generator (Gammel, 1998). For instance, the nature of the statistical distribution is relevant to ensure the positiveness of the scalar field to be generated (Malamud and Turcotte, 1999), and in that case log-normal, gamma or K-distributions are more suitable than Gaussian distributions. Nevertheless, since our analytical model is worked out in the Fourier space, and the calibration as well, which is of crucial importance, we shall check the consistency with a numerical model based on the fractional integration of white noise and introduced in App. A3.

Of course, spectral and fractal models are used not only in geophysics (Davis et al., 1994; Eneva, 1994; Main et al., 1999; Malamud and Turcotte, 1999; Southgate and Möller, 2000), but also in astrophysics (Labini et al., 1998; Stutzki et al., 1998), fluid mechanics (Mandelbrot, 1974; Scotti and Meneveau, 1999), biology (Peng et al., 1994; Buldyrev et al., 1995), medecine (Schlesinger and West, 1991; Chen et al., 1997; Geraets and van der Stelt, 2000; Ivanov et al., 2001; Echeverria et al., 2003), economics (Elliott, 1938; Mandelbrot, 1997; Ausloos et al., 1999), fine arts (Spehar et al., 2003; Hagerhall et al., 2004) and music (Voss and Clarke, 1978; Bulmer, 2000). In consequence, the results of the present paper can be hopefully applied to these fields of modelling.

We shall first proceed to the spectral analysis in Sect. 2 and fractal analysis in Sect. 3 and eventually propose a discussion of the consistency of both approaches in Sect. 4 and perspectives of this work in Sect. 5. The comparison with published results will be given thorough the paper along with commentaries of our own results.

2 Spectral analysis

2.1 Method

The usual way to get spectral components from the sampled measurements F_m of a function $F(x)$ is to apply a discrete Fourier transform (or FFT) in one dimension:

$$\tilde{F}(k) = \sum_{m=1}^{M} F_m e^{imk\Delta x} \qquad \text{with} \qquad F_m = F\,(m\Delta x) \tag{8}$$

and then take the amplitude:

$$S(k) = \left|\tilde{F}(k)\right|^2 . \tag{9}$$

For practical use, the discrete transform $F(k)$ is itself sampled:

$$\tilde{F}_n = \sum_{m=1}^{M} F_m e^{imn\Delta k\Delta x} \qquad \text{with} \qquad \tilde{F}_n = \tilde{F}\,(n\Delta k)\,. \tag{10}$$

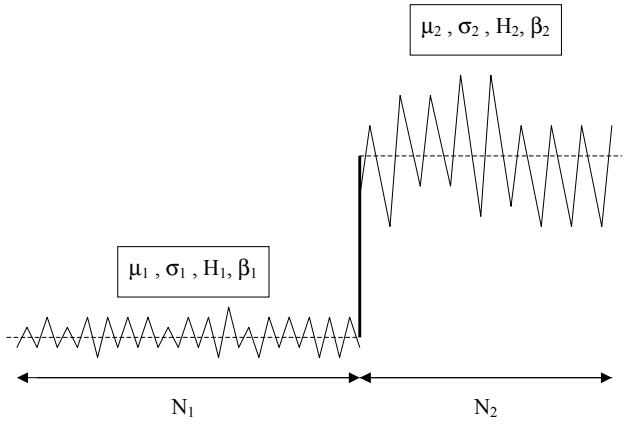

Fig. 1. Model of one-dimensional discontinuity between two homogeneous fractal media.

2.2 Analytical model

Now, in order to grasp how a discontinuity between two homogeneous regions 1 and 2 can alter the estimation of the spectral index, we have built up a one-dimensional model (see App. A1 for derivation of formulas). Region 1 may represent the background and region 2 a cloud. Let N_1, N_2 be the pixel numbers of regions 1 and 2, μ_1, μ_2 the mean levels, σ_1, σ_2 the standard deviations and β_1, β_2 the spectral indices of the fluctuating scalar fields F_1 and F_2 (Fig. 1). These may represent the temperature, the water content, the humidity for instance, and since these quantities are positive, the standard deviation σ should be smaller than the average μ. In the contrary, note that detrended data obtained by removing the average trend, usually by linear fitting (Chen et al., 2002), can also be described by our model with $\mu = 0$.

Let us first define the spectral form of the PSD. If we separate each of the scalar fields F_1 and F_2 in two components, an average μ_j and a fluctuating part G_j of zero mean and standard deviation σ_j ($j = 1, 2$) we can write:

$$F_j(x) = \mu_j + G_j(x) \text{ with } \begin{cases} \overline{G_j(x)} = 0 \\ \overline{G_j(x)^2} = \sigma_j^2 \end{cases} . \tag{11}$$

Then G_j cannot have a simple power-law spectrum $k^{-\beta j}$, like a self-affine fractal (Malamud and Turcotte, 1999), since it would have an infinite average. A compromise consists in defining the spectrum of G_j by:

$$\tilde{G}_j(k) = A_j\,(k)\,e^{i\Phi_j(k)} \text{ with } A_j\,(k) = \frac{a_j}{\left(k_0^2 + k^2\right)^{\beta_j/4}}, \tag{12}$$

where $\mathrm{A}_j(k)$ and $\Phi_j(k)$ are the amplitude and phase spectra respectively, k_0 is the outer scale wave number chosen equal to $\pi/(N\Delta x)$, and the constant a_j is found by normalisation of the PSD to σ_j^2. Note that we take equal outer scale wavenumbers $k_{01} = k_{02} = k_0$. With the reduced wave-number ξ, these quantities write:

$$\xi_0 = \frac{\pi}{N} \qquad a_j = \frac{N_j}{\sqrt{J(N_j, \xi_0, \beta_j)}}\sigma_j \tag{13}$$

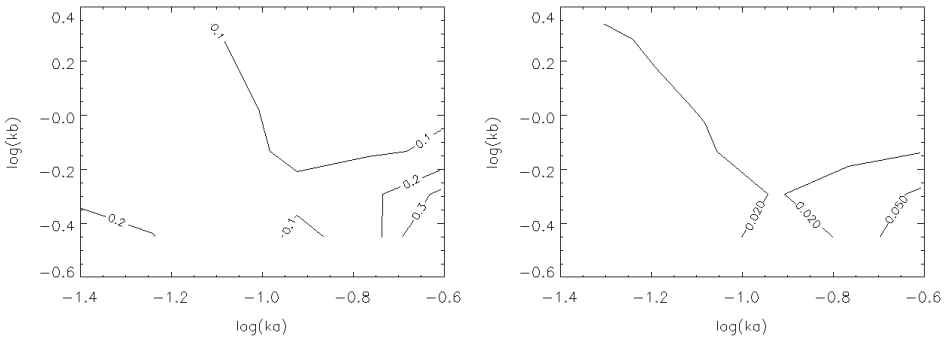

(a) $\mu = 5$, $\sigma = 1$, $\beta = 1$ *(b) $\mu = 10$, $\sigma = 5$, $\beta = 1$*

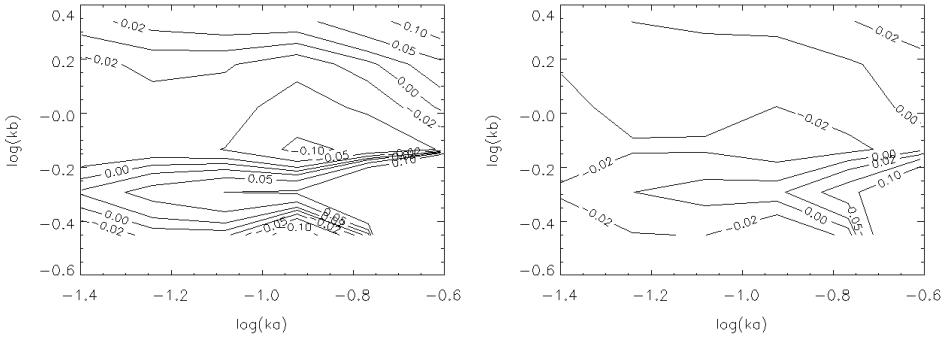

(c) $\mu = 5$, $\sigma = 1$, $\beta = 2$ *(d) $\mu = 10$, $\sigma = 5$, $\beta = 2$*

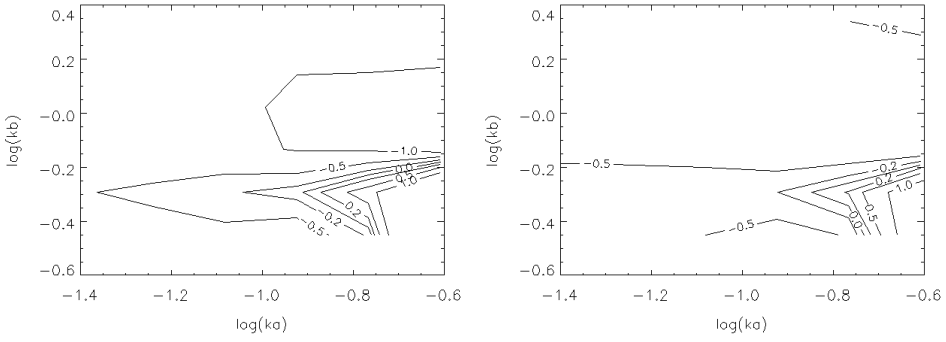

(e) $\mu = 5$, $\sigma = 1$, $\beta = 3$ *(f) $\mu = 10$, $\sigma = 5$, $\beta = 3$*

Fig. 2. Optimisation of the regression interval $[k_a, k_b]$. Plot of the difference $\beta_{est}-\beta$ between the true and the estimated spectral indices as a function of the bounds (k_a, k_b).

and:

$$J\left(N_j, \xi_0, \beta_j\right) = \sum_{n=0}^{N_j} \frac{1}{\left(\xi_0^2 + \xi_n^2\right)^{\beta_j/2}} \text{ where } \xi_n = \frac{n}{N}\xi_N. \quad (14)$$

The computation of the spectrum obtained by the superposition of those of media 1 and 2 eventually leads to the analytical PSD (App. A1):

$$\left|\tilde{F}\left(\xi\right)\right|^2 = \frac{(\mu_1-\mu_2)\left(\mu_1 \sin^2 \frac{N_1\xi}{2} - \mu_2 \sin^2 \frac{N_2\xi}{2}\right) + \mu_1\mu_2 \sin^2 \frac{N\xi}{2}}{\sin^2 \frac{\xi}{2}} + \frac{N_1^2}{J_1} \frac{\sigma_1^2}{\left(\xi_0^2+\xi^2\right)^{1+\beta_1/2}} + \frac{N_2^2}{J_2} \frac{\sigma_2^2}{\left(\xi_0^2+\xi^2\right)^{1+\beta_2/2}}, \quad (15)$$

where $N = N_1+N_2$. It depends on eight parameters N_1, N_2, μ_1, μ_2, σ_1, σ_2, β_1 and β_2. In relation (15), the first contribution is relative to the steady component (average) and the next two to the fluctuations about the average. It is important to keep in mind that it results from a compromise where

the Fourier transform of the steady component μ has been calculated on the bounded support, whereas that of the fluctuating component G has been approximated on an infinite support for the sake of analytical handiness (see App. A1). Therefore Fejer's kernels relative to the average will cause oscillations in the spectral plots whereas the fluctuating part of the spectrum will be smooth.

2.3 Validation

Before performing simulations and a parametric study of Eq. (15) we proceed to validating, or better, checking the consistency of our analytic model, especially as regards calibration, which is of crucial importance, with the numerical model of FBM based on Monte-Carlo and described in App. A3. For a unique medium, the expression (15) of the spectrum reduces to:

$$\left|\tilde{F}(\xi)\right|^2 = \mu^2 \frac{\sin^2 \frac{N\xi}{2}}{\sin^2 \frac{\xi}{2}} + \frac{N^2}{J} \frac{\sigma^2}{\left(\xi_0^2 + \xi^2\right)^{1+\beta/2}}. \quad (16)$$

Since the interval $[k_a, k_b]$ where the slope is estimated has some influence on the results, we determined the best fitting by plotting the difference $\Delta\beta = \beta_{est} - \beta$ between the true and the estimated spectral index as a function of the bounds (k_a, k_b) in six situations of the three parameters (μ, σ, β) (Fig. 2). From this figure, it comes out that the best fitting interval, given by the level curve $\Delta\beta = 0$, is about $[-0.8,+0.2]$ in the case $\beta = 2$. In other cases, the spectrum of raw data is contaminated by Fejer's kernel contribution and the fitting interval is not so relevant because the spectrum is rather straight. The actual bounds are therefore chosen as $\log_{10} k_a = -0.766$ and $\log_{10} k_b = 0.181$.

Examples of this analytical spectrum for a single medium sampled with one hundred points, together with a realisation of the numerical spectra possessing the same μ, σ, β sampled with one thousand points ($N = 1000$) are shown on Fig. 3. The sampling of our analytical model is exponential whereas that of the numerical realisation is linear.

The agreement between both models seems quite satisfying, as regards levels and slopes. The two situations of raw data (Fig. 3, left side) and detrended data (Fig. 3, right side) are displayed. Note that when $\mu/\sigma \geq 1$, the fluctuation component is larger than the steady component and the estimation of β is altered whereas when $\mu/\sigma \ll 1$, $\mu = 0$ in the limit of detrended data, the fractal component is predominant and the true β is ideally retrieved. In the former case, the first term in Eq. (16), Fejer's Kernel, is dominant and since it admits as envelope the equivalent expression:

$$\left|\tilde{F}(\xi)\right|^2 \propto 4\frac{\mu^2}{\xi^2} \quad (17)$$

we conclude that the slope of the spectrum tends towards -2 (Rustom and Bélair, 1997). As could be also expected, even for detrended data ($\mu = 0$) the numerical spectrum oscillates at small scales whereas our analytical spectrum does not (Figs. 3b, d, f and 4e), since we kept the smoothed fluctuation spectrum unconvolved with Dirichlet kernel (see App. A1, Eq. A12 instead of Eq. A10).

2.4 Simulations

The influence of the eight parameters N_1, N_2, μ_1, μ_2, σ_1, σ_2, β_1 and β_2 can be now examined. The analytic spectra defined by relation (15) are sampled with one hundred points and the slope $-\beta$ is computed (β_{est}) between the bounds chosen in the previous subsection (Fig. 4). On the same figure, the numerical FBM is illustrated with $N = 1000$. As we shall see in Sect. 3, more points are necessary to the fitting of the spectral curves (31 points) as compared to that of roughness curves (6 points) because of oscillations present in the spectra at middle scales, caused by Fejer's kernels due to the contribution of average in relation (15). The size of the samples ($N = 100$, 1000, 10 000) has been chosen in relation with the analysis of real data performed in standard works.

In double logarithmic scales the curves have approximately straight decreasing parts at small and middle scales, so that straight lines can be fitted to them, and β be estimated (Fig. 4). The interplay between the contribution due to Fejer's kernels (envelope slope close to -2) and the fractal spectrum causes large discrepancies except with detrented data (Fig. 4e). For raw data this leads to underestimating β and to non-monotonous variations of β as a function of parameters.

Assuming that region 1 is the background and region 2 is the structure under study, we distinguished on the one hand two cases due to a gap of the statistical parameters μ and σ (monofractal discontinuity): a) a μ-type, consisting in a gap of μ only, with all other parameters unchanged; b) a σ-type, consisting in a gap of σ only, with all other parameters unchanged ($\mu > \sigma$)

and a special, detrended, σ-type, with only a gap of σ and $\mu_1 = \mu_2 = 0$.

The spectral index is chosen as describing typically:
a) anti-correlated (A) or anti-persistent fluctuations ($\beta = 1$);
b) non-correlated (N) fluctuations ($\beta = 2$);
c) correlated (C) or persistent fluctuations ($\beta = 3$).

On the other hand we distinguish three cases due to a gap in the spectral index β (true bifractal discontinuity):
a) an A-N case, consisting in two regions ($\beta_1 = 1$; $\beta_2 = 2$) with same (μ, σ);
b) an N-C case, consisting in two regions ($\beta_1 = 2$; $\beta_2 = 3$) with same (μ, σ);
c) an A-C case, consisting in two regions ($\beta_1 = 1$; $\beta_2 = 3$) with same (μ, σ).

In the monofractal cases (Figs. 5a, c, e), the discontinuity is due to a gap of μ, σ on raw data (solid and dotted lines) or only σ on detrended data (dashed line). As pointed out above, Fejer's kernels produce sidelobes in the total spectrum which are reflected in oscillations on the $\beta(N_2/N)$ plot when $\mu_1 \neq \mu_2$ and they are enhanced as the ratio μ/σ increases. They become smoother as $\beta \to 1$ because the fractal spectrum has then a smaller slope and it is therefore above the steady component spectrum if μ/σ is large enough (Fig. 5a).

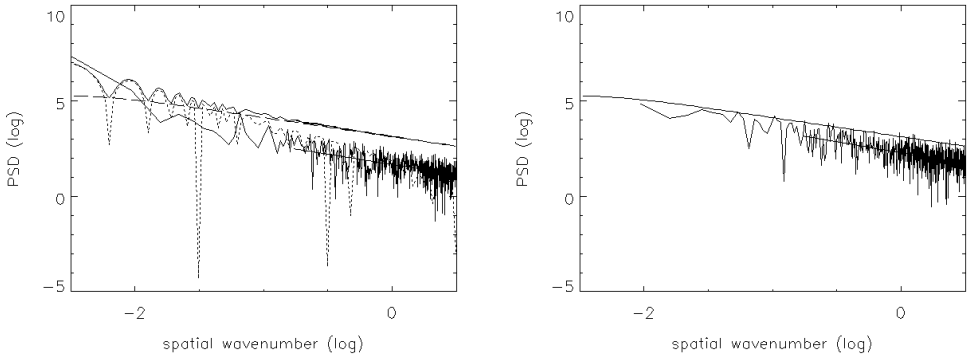

(a) $\mu = 5$; $\sigma = 1$; $\beta = 1$; $\beta_{est\ an} = 1.087$; $\beta_{est\ num} = 1.061$

(b) $\mu = 0$; $\sigma = 1$; $\beta = 1$; $\beta_{est\ an} = 1.000$; $\beta_{est\ num} = 1.158$

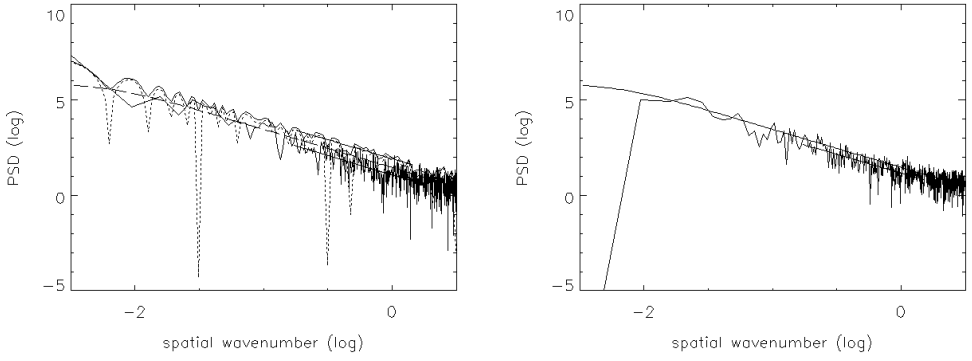

(c) $\mu = 5$; $\sigma = 1$; $\beta = 2$; $\beta_{est\ an} = 1.989$; $\beta_{est\ num} = 2.037$

(d) $\mu = 0$; $\sigma = 1$; $\beta = 2$; $\beta_{est\ an} = 2.000$; $\beta_{est\ num} = 1.952$

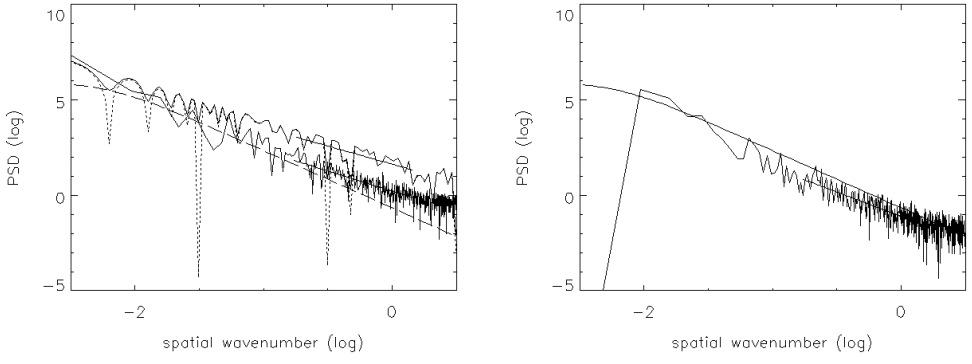

(e) $\mu = 5$; $\sigma = 1$; $\beta = 3$; $\beta_{est\ an} = 1.893$; $\beta_{est\ num} = 2.107$

(f) $\mu = 0$; $\sigma = 1$; $\beta = 3$; $\beta_{est\ an} = 2.999$; $\beta_{est\ num} = 2.543$

Fig. 3. Comparison of Power-Spectral Density (PSD) profiles for a single medium (N = 1000) as given by the analytical formula (16) (solid smooth or upper curve) and as calculated from a realisation of the numerical FBM, App. A3 (solid wavy curve) with raw data (left) and detrended data (right). For the analytical model, the individual PSD contributions due to Fejer'kernel (dotted) and the fluctuations (dashed) are also plotted.

On the opposite when $\beta \to 3$ oscillations are stronger and there is some kind of saturation effect since the estimated β does not grow larger than 2.4 (Fig. 5e). These curves are getting smoother as N increases (compare top, middle and bottom curves).

In the purely bifractal cases (Figs. 5 b, d, f), the discontinuity is due essentially to a gap of β. The oscillations are still contaminating the results though a trend is clearly shown by the curve $\mu_1 = \mu_2$ (dotted line) growing monotonously from β_1 to β_2 as N_2 goes up to N. Detrended data (μ = 0) produce

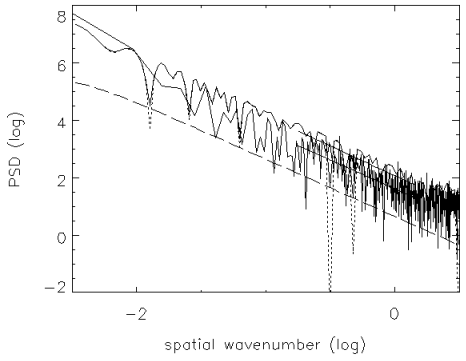

(a) $\mu_1 = 5$; $\mu_2 = 10$; $\sigma_1 = 1$; $\sigma_2 = 1$; $\beta_1 = 2$; $\beta_2 = 2$; $\beta_{est\ an} = 2.081$; $\beta_{est\ num} = 2.006$

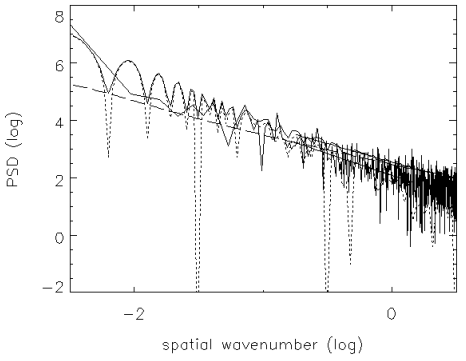

(b) $\mu_1 = 5$; $\mu_2 = 5$; $\sigma_1 = 1$; $\sigma_2 = 1$; $\beta_1 = 1$; $\beta_2 = 2$; $\beta_{est\ an} = 1.284$; $\beta_{est\ num} = 1.518$

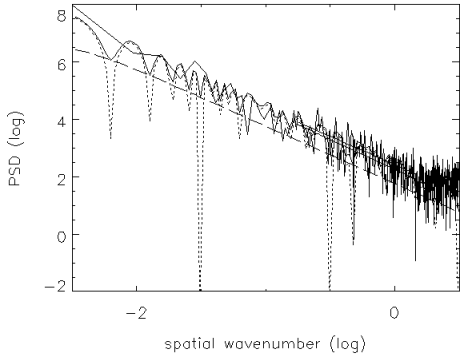

(c) $\mu_1 = 10$; $\mu_2 = 10$; $\sigma_1 = 1$; $\sigma_2 = 5$; $\beta_1 = 2$; $\beta_2 = 2$; $\beta_{est\ an} = 1.979$; $\beta_{est\ num} = 2.070$

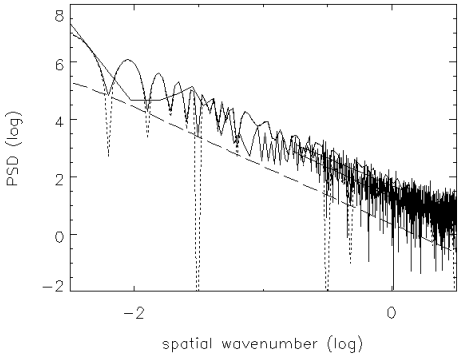

(d) $\mu_1 = 5$; $\mu_2 = 5$; $\sigma_1 = 1$; $\sigma_2 = 1$; $\beta_1 = 2$; $\beta_2 = 3$; $\beta_{est\ an} = 1.927$; $\beta_{est\ num} = 2.114$

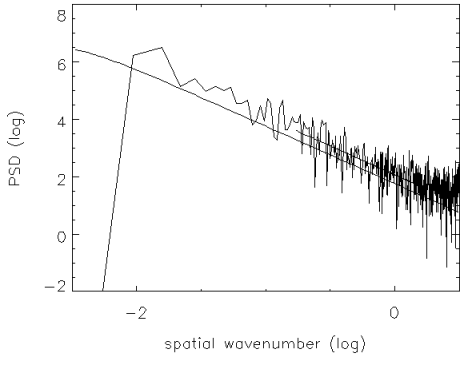

(e) $\mu_1 = 0$; $\mu_2 = 0$; $\sigma_1 = 1$; $\sigma_2 = 5$; $\beta_1 = 2$; $\beta_2 = 2$; $\beta_{est\ an} = 2.000$; $\beta_{est\ num} = 2.005$

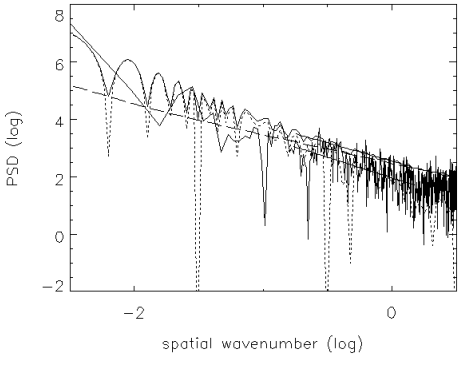

(f) $\mu_1 = 5$; $\mu_2 = 5$; $\sigma_1 = 1$; $\sigma_2 = 1$; $\beta_1 = 1$; $\beta_2 = 3$; $\beta_{est\ an} = 1.276$; $\beta_{est\ num} = 1.433$

Fig. 4. Examples of Power-Spectral Density (PSD) profiles for monofractal (left) and bifractal (right) discontinuities ($N_1 = N_2 = 500$) as given by the analytical formula (15) (solid smooth or upper curve) and as calculated from a realisation of the numerical FBM, App. A3 (solid wavy curve).

ideal variations of the estimated β (dashed lines) since the contribution of the steady component is removed, and only the mixing of the pure fractal spectra comes into play. The function $\beta(N_2/N)$ is either constant for the monofractal dis-

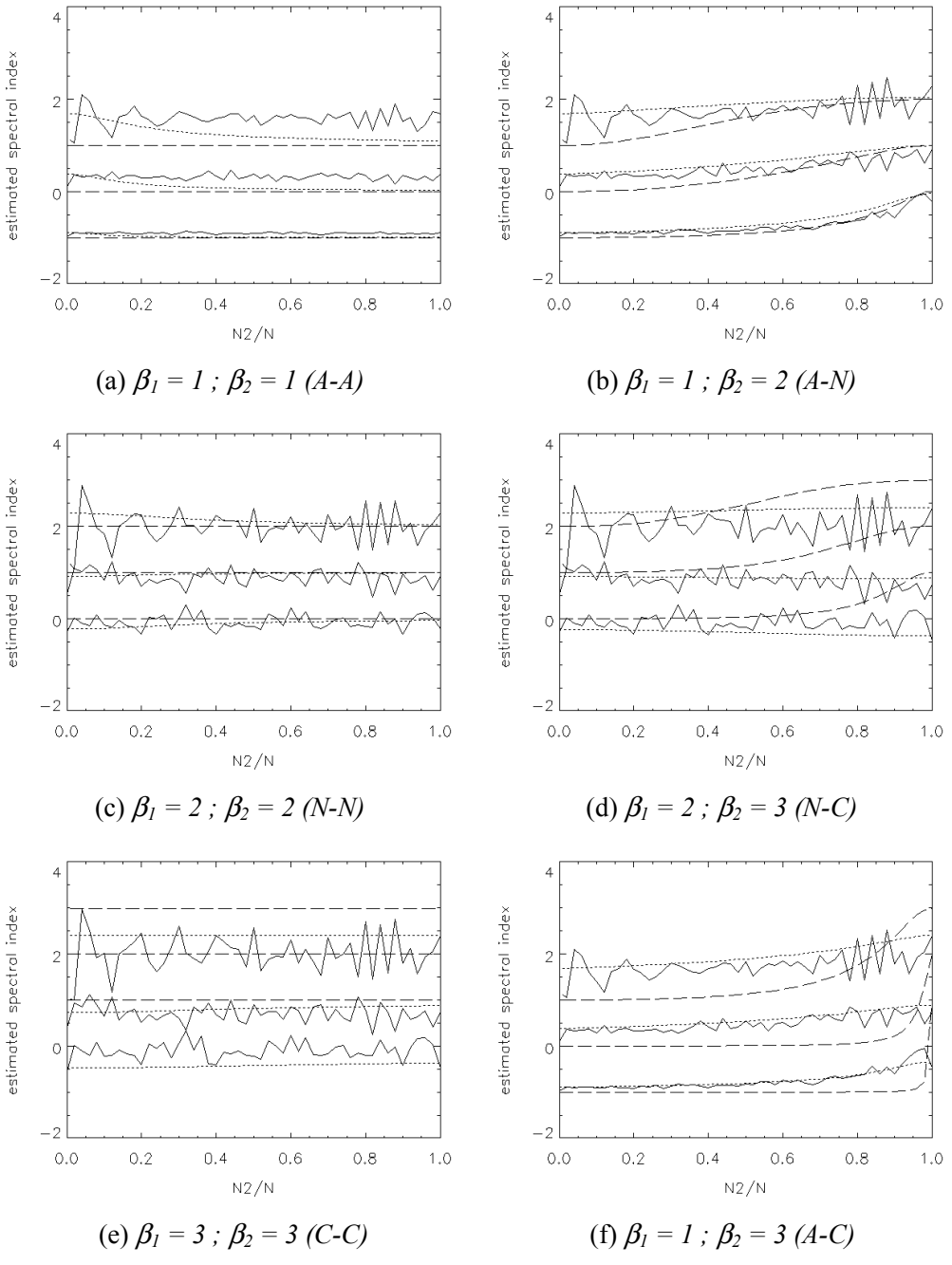

(a) $\beta_1 = 1$; $\beta_2 = 1$ (A-A)

(b) $\beta_1 = 1$; $\beta_2 = 2$ (A-N)

(c) $\beta_1 = 2$; $\beta_2 = 2$ (N-N)

(d) $\beta_1 = 2$; $\beta_2 = 3$ (N-C)

(e) $\beta_1 = 3$; $\beta_2 = 3$ (C-C)

(f) $\beta_1 = 1$; $\beta_2 = 3$ (A-C)

Fig. 5. Variations of the estimated spectral index β as a function of the relative structure size N_2/N in the μ, σ and detrended cases for monofractal (left) and bifractal (right) discontinuities. In each plot, N = 100 (upper curves), N = 1000 (middle curves) and N = 10 000 (lower curves); the middle and lower curves are shifted downwards by -1 and -2, respectively to avoid confusion. μ_1 = 5; μ_2 = 10; σ_1 = 1; σ_2 = 1 (solid line). μ_1 = 10; μ_2 = 10; σ_1 = 1; σ_2 = 5 (dotted line). μ_1 = 0; μ_2 = 0; σ_1 = 1; σ_2 = 5 (dashed line).

continuity or increasing for the bifractal discontinuity. Note that in this latter case, the medium with smaller σ is predominant ($\sigma_1 < \sigma_2$) and steepens the increase as $N_2/N \to 1$.

For a monofractal discontinuity, the influence of (β_1, β_2) such that $\beta_1 = \beta_2$ is also investigated with $N_1 = N_2 = N/2$ (Fig. 6). It appears that β is overestimated if $\beta < 2$ (Fig. 6b) much more for a μ-gap with an amount $\Delta\beta$ = 0.2 (N = 10 000) to $\Delta\beta$ = 0.7 (N = 100), than for a σ-gap with $\Delta\beta$ = 0.05 (N = 10 000) to $\Delta\beta$ = 0.2 (N = 100). Of course the saturation effect mentioned before occurs for $\beta > 2$ in any (μ,σ) situation, even when $\mu_1 \approx \mu_2$, since Fejer's kernel is still present, although weighted by the product $\mu_1\mu_2$:

$$\left|\tilde{F}(\xi)\right|^2 = \mu_1\mu_2 \frac{\sin^2\frac{N\xi}{2}}{\sin^2\frac{\xi}{2}} + \frac{N_1^2}{J_1}\frac{\sigma_1^2}{\left(\xi_0^2+\xi^2\right)^{1+\beta_1/2}} + \frac{N_2^2}{J_2}\frac{\sigma_2^2}{\left(\xi_0^2+\xi^2\right)^{1+\beta_2/2}}. \quad (18)$$

Thus the influence of Fejer's kernel is perfectly cancelled out if and only if $\mu_1 = \mu_2 = 0$ (Fig. 6c) and this property may justify trend-corrected methods such as the Detrended Fluctuation Analysis (DFA).

For a bifractal discontinuity, the influence of β_2 when β_1 is kept constant is investigated with $N_1 = N_2 = N/2$ (Fig. 7). The medium with anti-correlated fluctuations ($\beta_1 = 1$) is clearly predominant (Figs. 7a, c). This can be explained by the fact that its slope being smaller, the spectrum will have relatively more energy at middle scales. Nevertheless, for raw data ($\mu \neq 0$) a saturation effect due to Fejer's kernel adds up when $\beta_1 \gg 2$ (Fig. 7e). In any case the curves intersect the diagonal ideally for large N at $\beta_1 = \beta_2$, i.e. where the whole sample is monofractal, and the overestimation $\Delta\beta$ amounts 0.2 (N = 10 000) up to 0.7 (N = 100).

3 Fractal analysis

3.1 Method

The box counting method, which will be applied here, consists in computing the standard deviation σ of data in a gliding box of constant size L, then taking the ensemble average $\overline{\sigma}$ of σ. By repeating the operation for different sizes L, we can plot the function $\overline{\sigma} = f(L)$. In simple situations, it can be modelled by a power law:

$$\overline{\sigma}(L) = \sigma_0 \left(\frac{L}{L_0}\right)^H \tag{19}$$

and the slopes of straight parts in double logarithmic scales yield the scaling exponent H, the so-called Hurst parameter, related to the fractal dimension D by (Moghaddam et al., 1991):

$$H = E + 1 - D, \tag{20}$$

where E is the topological dimension. This is an approximation which does not hold for certain classes of processes (Gneiting and Schlather, 2004). Actually H describes the asymptotic behaviour at large correlation distances whereas D scales the growing rate at small distances.

Let us mention by the way that a monofractal structure should be characterised not only by its fractal dimension (or Hurst exponent) but also by its lacunarity Λ through a box counting or moments method (Mandelbrot, 1982; Moghaddam et al., 1991; Blumenfeld and Mandelbrot, 1997; Domon and Honda, 1999) or the dilation method (Domon and Honda, 1999). Unfortunately, this quantity is a function $\Lambda(L)$ of the box size L and, so far as we know, no link with the lacunarity parameter γ in expressions (4) and (5) has yet been proposed. Therefore we shall restrict ourselves to the roughness analysis.

3.2 Analytical model

As a complement information to the spectral analysis it is important to study the influence of a discontinuity on the estimation of the roughness parameter H. In that purpose, a one-dimensional analytical model has been built up and the details of its derivation are described in App. A2. Let N_1, N_2 be the pixel numbers in regions 1 and 2, μ_1, μ_2 the mean levels, σ_1, σ_2 the standard deviations and H_1, H_2 the Hurst parameters of the fluctuating scalar fields F_1 and F_2 (Fig. 1). Like in the spectral analysis we shall make the distinction between raw ($\mu \neq 0$) and detrended ($\mu = 0$) data.

For a normalised box size containing L pixels, the average standard deviation in the box through scanning of each of the

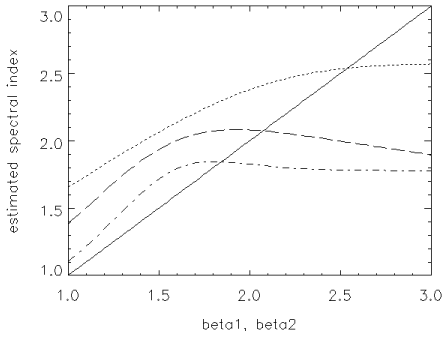

(a) $\mu_1 = 5$; $\mu_2 = 10$; $\sigma_1 = 1$; $\sigma_2 = 1$

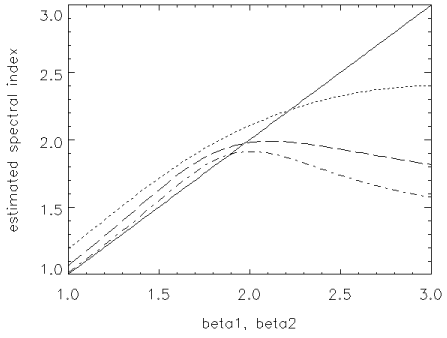

(b) $\mu_1 = 10$; $\mu_2 = 10$; $\sigma_1 = 1$; $\sigma_2 = 5$

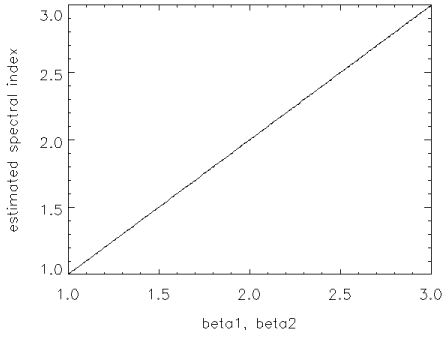

(c) $\mu_1 = 0$; $\mu_2 = 0$; $\sigma_1 = 1$; $\sigma_2 = 5$

Fig. 6. Variations of the estimated spectral index β as a function of the spectral index $\beta_1 = \beta_2$ (monofractal discontinuity) for raw **(a)**, **(b)** and detrended **(c)** data. In each plot, N = 100, $N_1 = N_2$ = 50 (dotted line), N = 1000, $N_1 = N_2$ = 500 (dashed line), N = 10 000, $N_1 = N_2$ = 5000 (dotted-dashed line) and diagonal $\beta = \beta_1$ (solid line).

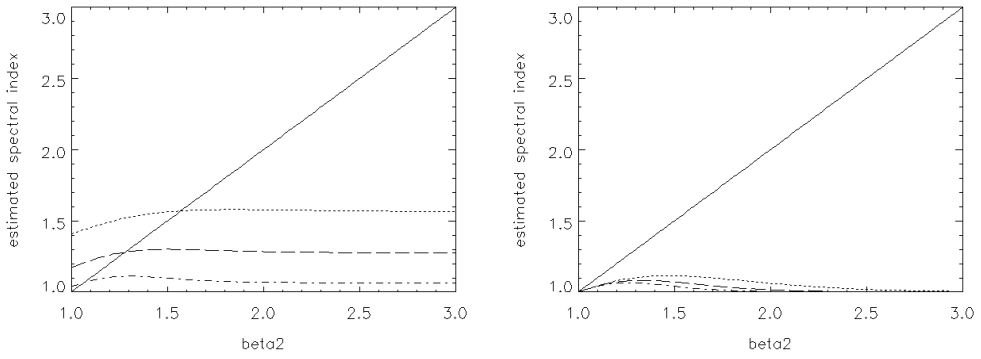

(a) $\mu_1 = 5$; $\mu_2 = 5$; $\sigma_1 = 1$; $\sigma_2 = 1$; $\beta_1 = 1$

(b) $\mu_1 = 0$; $\mu_2 = 0$; $\sigma_1 = 1$; $\sigma_2 = 1$; $\beta_1 = 1$

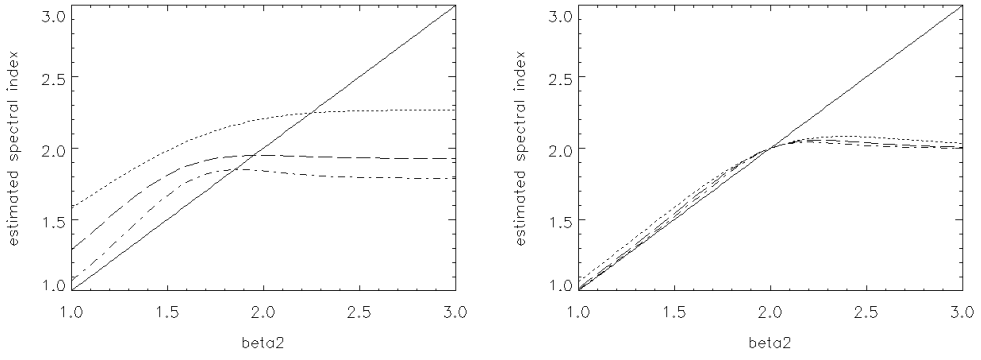

(c) $\mu_1 = 5$; $\mu_2 = 5$; $\sigma_1 = 1$; $\sigma_2 = 1$; $\beta_1 = 2$

(d) $\mu_1 = 0$; $\mu_2 = 0$; $\sigma_1 = 1$; $\sigma_2 = 1$; $\beta_1 = 2$

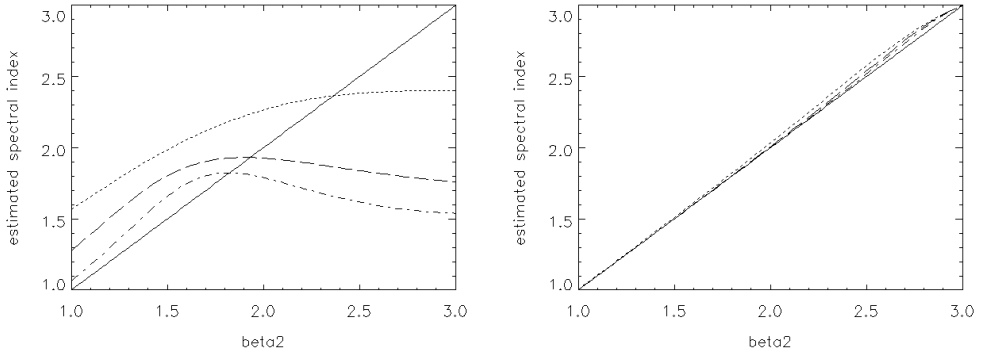

(e) $\mu_1 = 5$; $\mu_2 = 5$; $\sigma_1 = 1$; $\sigma_2 = 1$; $\beta_1 = 3$

(f) $\mu_1 = 0$; $\mu_2 = 0$; $\sigma_1 = 1$; $\sigma_2 = 1$; $\beta_1 = 3$

Fig. 7. Variations of the estimated spectral index β as a function of the spectral index β_2 (bifractal discontinuity) for raw (left) and detrended (right) data. In each plot, N = 100, $N_1 = N_2$ = 50 (dotted line), N = 1000, $N_1 = N_2$ = 500 (dashed line), N = 10 000, $N_1 = N_2$ = 5000 (dotted-dashed line) and diagonal $\beta = \beta_1$ (solid line).

regions is given by the expressions:

$$\overline{\sigma}(L) = \sigma_1 \left(\frac{L}{N_1}\right)^{H_1} \qquad \overline{\sigma}(L) = \sigma_2 \left(\frac{L}{N_2}\right)^{H_2} \tag{21}$$

and for the global data by the expressions (App. A2):

a) if $0 \leq L \leq \min(N_1, N_2)$

$$(N-L+1)\overline{\sigma}(L) = \sum_{n=1}^{L-1} \sqrt{\frac{n}{L}\sigma_1^2 \left(\frac{L}{N_1}\right)^{2H_1} + \left(1-\frac{n}{L}\right)\sigma_2^2 \left(\frac{L}{N_2}\right)^{2H_2} + \frac{n}{L}\left(1-\frac{n}{L}\right)(\mu_1-\mu_2)^2}$$

$$+\sigma_1(N_1+1-L)\left(\frac{L}{N_1}\right)^{H_1}+\sigma_2(N_2+1-L)\left(\frac{L}{N_2}\right)^{H_2} \quad (22)$$

b) if $\max(N_1, N_2) \le L \le N$

$$(N-L+1)\overline{\sigma}(L) = \sum_{n=1}^{N-L+1}\sqrt{\frac{n}{L}\sigma_1^2\left(\frac{L}{N_1}\right)^{2H_1}+\left(1-\frac{n}{L}\right)\sigma_2^2\left(\frac{L}{N_2}\right)^{2H_2}+\frac{n}{L}\left(1-\frac{n}{L}\right)(\mu_1-\mu_2)^2} \quad (23)$$

c) if $\min(N_1, N_2) \le L \le \max(N_1, N_2)$ and $N_1 < N_2$

$$(N-L+1)\overline{\sigma}(L) = \sum_{n=1}^{N_1}\sqrt{\frac{n}{L}\sigma_1^2\left(\frac{L}{N_1}\right)^{2H_1}+\left(1-\frac{n}{L}\right)\sigma_2^2\left(\frac{L}{N_2}\right)^{2H_2}+\frac{n}{L}\left(1-\frac{n}{L}\right)(\mu_1-\mu_2)^2} \quad (24)$$
$$+\sigma_2(N_2+1-L)\left(\frac{L}{N_2}\right)^{H_2}$$

d) if $\min(N_1, N_2) \le L \le \max(N_1, N_2)$ and $N_2 < N_1$

$$(N-L+1)\overline{\sigma}(L) = \sum_{n=1}^{N_2}\sqrt{\frac{n}{L}\sigma_1^2\left(\frac{L}{N_1}\right)^{2H_1}+\left(1-\frac{n}{L}\right)\sigma_2^2\left(\frac{L}{N_2}\right)^{2H_2}+\frac{n}{L}\left(1-\frac{n}{L}\right)(\mu_1-\mu_2)^2} \quad (25)$$
$$+\sigma_1(N_1+1-L)\left(\frac{L}{N_1}\right)^{H_1}$$

with the trivial cases

$$\text{e) if } N_1 = 0: \qquad \overline{\sigma}(L) = \sigma_2\left(\frac{L}{N}\right)^{H_2} \quad (26)$$

and

$$\text{f) if } N_2 = 0: \qquad \overline{\sigma}(L) = \sigma_1\left(\frac{L}{N}\right)^{H_1}. \quad (27)$$

At "small" scales, which are described by expression (22), the sum of the first term represents the discontinuity, whereas the other two terms represent the textures of media 1 et 2 separately. At "large" scales, which are described by expression (23), there only remains the contribution of the discontinuity because, in that case, the discontinuity always lies within the gliding box. The intermediate scales are described by expressions (24) and (25), and the limit cases by expressions (26) and (27).

3.3 Validation

Before performing simulations and a parametric study of relations (22)–(27) we proceed, like in the spectral analysis, to checking the consistency of our analytic model, mainly as regards calibration, with the numerical model of FBM described in App. A3. Note that for a unique medium, the expressions (22)–(27) reduce to:

$$\overline{\sigma}(L) = \sigma_0\left(\frac{L}{N}\right)^{H}. \quad (28)$$

The bounds (L_a, L_b) of the linear regression interval have been chosen in consistency with those (k_a, k_b) of the spectral analysis (Sect. 2.3) such that:

$$k_a L_a = 2\pi \qquad k_b L_b = 2\pi. \quad (29)$$

The actual bounds, compatible with relations (29) and the exponential L-sampling, are therefore chosen as $\log_{10} L_a = 0.632$ and $\log_{10} L_b = 1.579$.

Examples of this analytical model are plotted on Fig. 8, together with the roughness graph of a realisation of the FBM possessing the same μ, σ, β (same cases as with Fig. 3). The agreement between both models seems quite satisfying, as regards levels and slopes, except for the slope when H approaches zero. As we explained in App. A3, this behaviour is not really a difficulty here since we are interested in validating first of all the calibration, i.e. the function levels, and the slopes in most of the cases. Note that these graphs are not contaminated with oscillations, either for raw (Fig. 8, left side) or detrended (Fig. 8, right side) data.

3.4 Simulations

A sensitivity analysis to the parameters of the analytical model can be now performed. Indeed, expressions (22)–(25) show that whenever $\mu_1 \neq \mu_2$ only the ratios $\sigma_1/|\mu_1-\mu_2|$ and $\sigma_2/|\mu_1-\mu_2|$ are relevant, rather than μ_1, μ_2, σ_1 and σ_2 separately. Therefore, we may define the dimensionless ratios $(\mu_1 \neq \mu_2)$:

$$r_1 = \frac{\sigma_1}{|\mu_1-\mu_2|} \qquad r_2 = \frac{\sigma_2}{|\mu_1-\mu_2|} \quad (30)$$

and reduce the number of degrees of freedom to six: N_1, N_2, r_1, r_2, H_1, H_2 wherever $N_1 \neq 0$ and $N_2 \neq 0$. Nevertheless, for the sake of consistency with the spectral approach, we shall deal with the same parameter sets (μ, σ) as in Sect. 2.4. Note that when μ_1 is equal to μ_2, the expression under the square root reduces to the ordinary superposition rule (Chen et al., 2002) and does not depend on μ_1, μ_2 any more.

The analytic spectra are sampled with only twenty points and the slope H is computed (H_{est}) between the bounds (6 points) chosen in the previous subsection (Fig. 10). The reasons for that are essentially:
– oscillations are present in the PSD (15) but not in the roughness function (22)–(27);
– there is a slope change on roughness curves for windows of large size (log L > 2.5).

These profiles have nearly straight increasing parts at small and middle scales, so that straight lines can be fitted to them. Even in monofractal cases, H is much overestimated when there is a μ-gap $|\mu_1 - \mu_2|$ (Fig. 9a) and less with a σ-gap $|\sigma_1 - \sigma_2|$ (Fig. 9b). At large scales, curves generally have a maximum and a decreasing part. It should be noted that also in the bifractal case (Fig. 9, right) the curve has an extended inertial range for log L <2.5: the H-estimator sees the global structure as if it were homogeneous, i.e. as a monofractal.

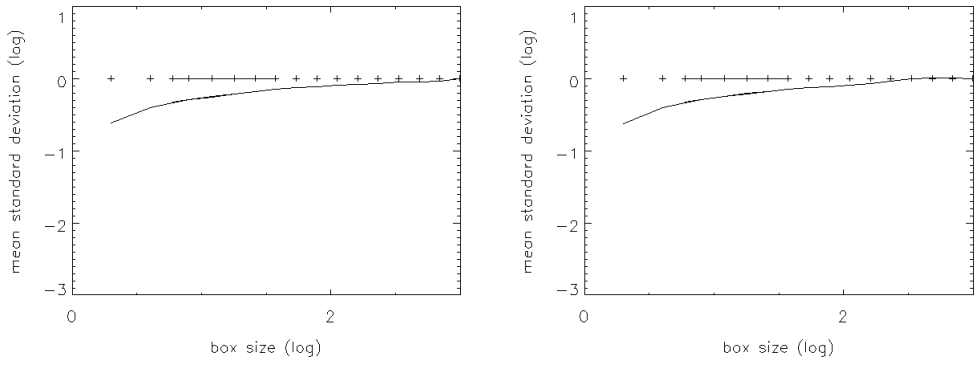

(a) $\mu = 5$; $\sigma = 1$; $H = 0$;
$H_{est\ an} = 0.000$; $H_{est\ num} = 0.228$

(b) $\mu = 0$; $\sigma = 1$; $H = 0$;
$H_{est\ an} = 0.000$; $H_{est\ num} = 0.225$

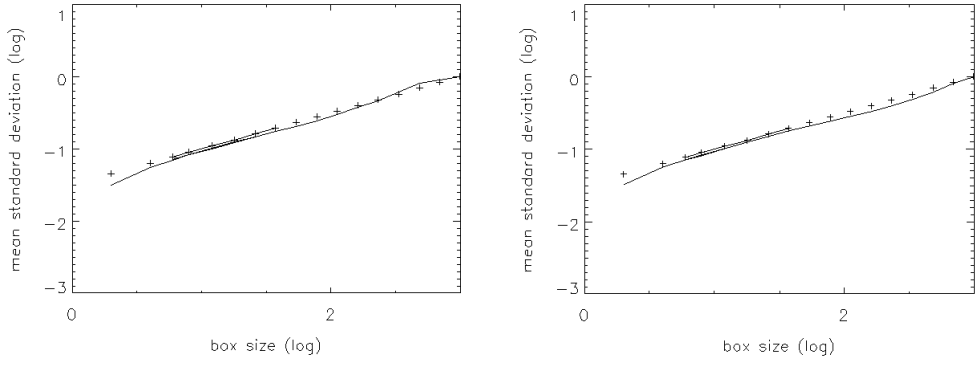

(c) $\mu = 5$; $\sigma = 1$; $H = 0.5$;
$H_{est\ an} = 0.500$; $H_{est\ num} = 0.495$

(d) $\mu = 0$; $\sigma = 1$; $H = 0.5$;
$H_{est\ an} = 0.500$; $H_{est\ num} = 0.512$

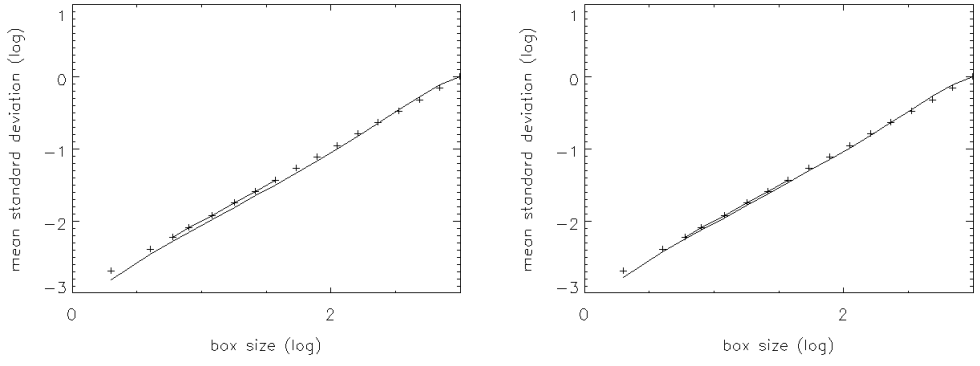

(e) $\mu = 5$; $\sigma = 1$; $H = 1$;
$H_{est\ an} = 1.000$; $H_{est\ num} = 0.997$

(f) $\mu = 0$; $\sigma = 1$; $H = 1$;
$H_{est\ an} = 1.000$; $H_{est\ num} = 0.989$

Fig. 8. Comparison of roughness graphs for a single medium as given by the analytical formulas (22)–(27) (crosses) and as calculated from a realisation of the numerical FBM, App. A3 (solid curve) (N = 1000) with raw data (left) and detrended data (right). Same cases as Fig. 3.

When one of the two media has anti-correlated fluctuations (H_1 = 0), the curve exhibits a kind of crossover at large scales and becomes slightly steeper (Figs. 9b, f). This is in perfect agreement with another published approach based on DFA (Chen et al., 2002). Note that unlike in the spectral approach, the analysis of raw data without μ-gap ($\mu_1 = \mu_2$) or detrended data (μ = 0) will give the same result (Figs. 9c, e) as could be expected from relations (22)–(25).

We assumed again that region 1 is the background, region 2 is the structure under study, and we distinguished the two monofractal cases (gap in μ and σ) like in the spectral analysis. The fractal scaling exponent is chosen as describing:
a) anti-correlated (A) or anti-persistent fluctuations (H = 0);
b) non-correlated (N) fluctuations (H = 1/2);

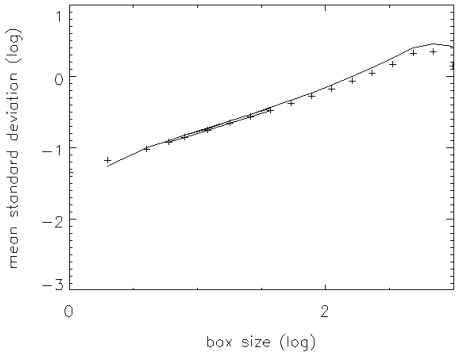

(a) $\mu_1 = 5$; $\mu_2 = 10$; $\sigma_1 = 1$; $\sigma_2 = 1$; $H_1 = 0.5$; $H_2 = 0.5$; $H_{est\ an} = 0.568$; $H_{est\ num} = 0.579$

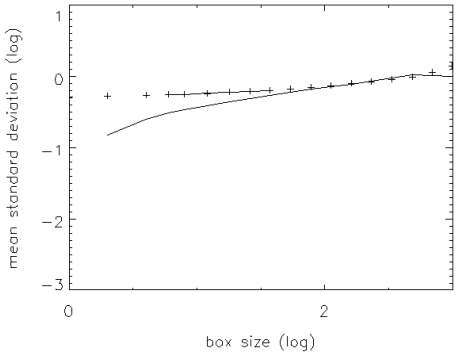

(b) $\mu_1 = 5$; $\mu_2 = 5$; $\sigma_1 = 1$; $\sigma_2 = 1$; $H_1 = 0$; $H_2 = 0.5$; $H_{est\ an} = 0.076$; $H_{est\ num} = 0.306$

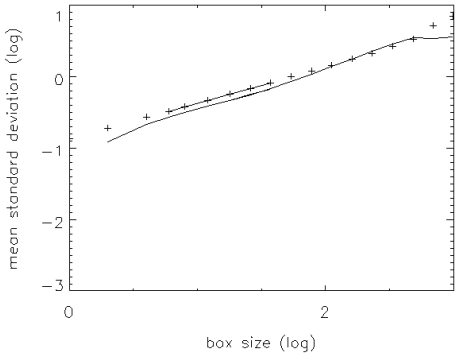

(c) $\mu_1 = 10$; $\mu_2 = 10$; $\sigma_1 = 1$; $\sigma_2 = 5$; $H_1 = 0.5$; $H_2 = 0.5$; $H_{est\ an} = 0.503$; $H_{est\ num} = 0.495$

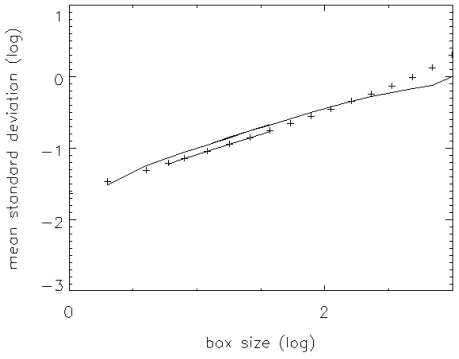

(d) $\mu_1 = 5$; $\mu_2 = 5$; $\sigma_1 = 1$; $\sigma_2 = 1$; $H_1 = 0.5$; $H_2 = 1$; $H_{est\ an} = 0.576$; $H_{est\ num} = 0.580$

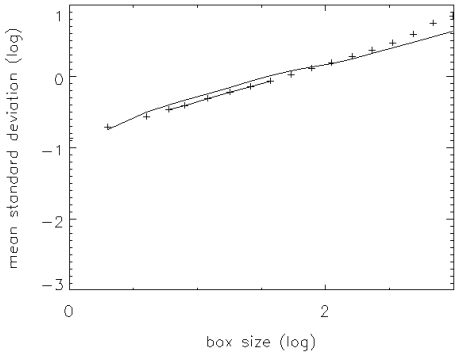

(e) $\mu_1 = 0$; $\mu_2 = 0$; $\sigma_1 = 1$; $\sigma_2 = 5$; $H_1 = 0.5$; $H_2 = 0.5$; $H_{est\ an} = 0.503$; $H_{est\ num} = 0.502$

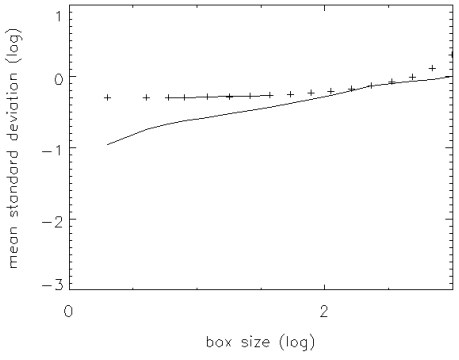

(f) $\mu_1 = 5$; $\mu_2 = 5$; $\sigma_1 = 1$; $\sigma_2 = 1$; $H_1 = 0$; $H_2 = 1$; $H_{est\ an} = 0.036$; $H_{est\ num} = 0.289$

Fig. 9. Examples of roughness graphs for monofractal (left) and bifractal (right) discontinuities ($N_1 = N_2 = 500$) as given by the analytical formulas (22)–(27) (crosses) and as calculated from a realisation of the numerical FBM, App. A3 (solid curve) ($N = 1000$). Same cases as Fig. 4.

c) correlated (C) or persistent fluctuations ($H = 1$).

On the other hand we define three cases due to a gap in the fractal index H (true bifractal discontinuity):

a) an A-N case, consisting in two regions ($H_1 = 0$; $H_2 = 1/2$) with same (μ,σ);

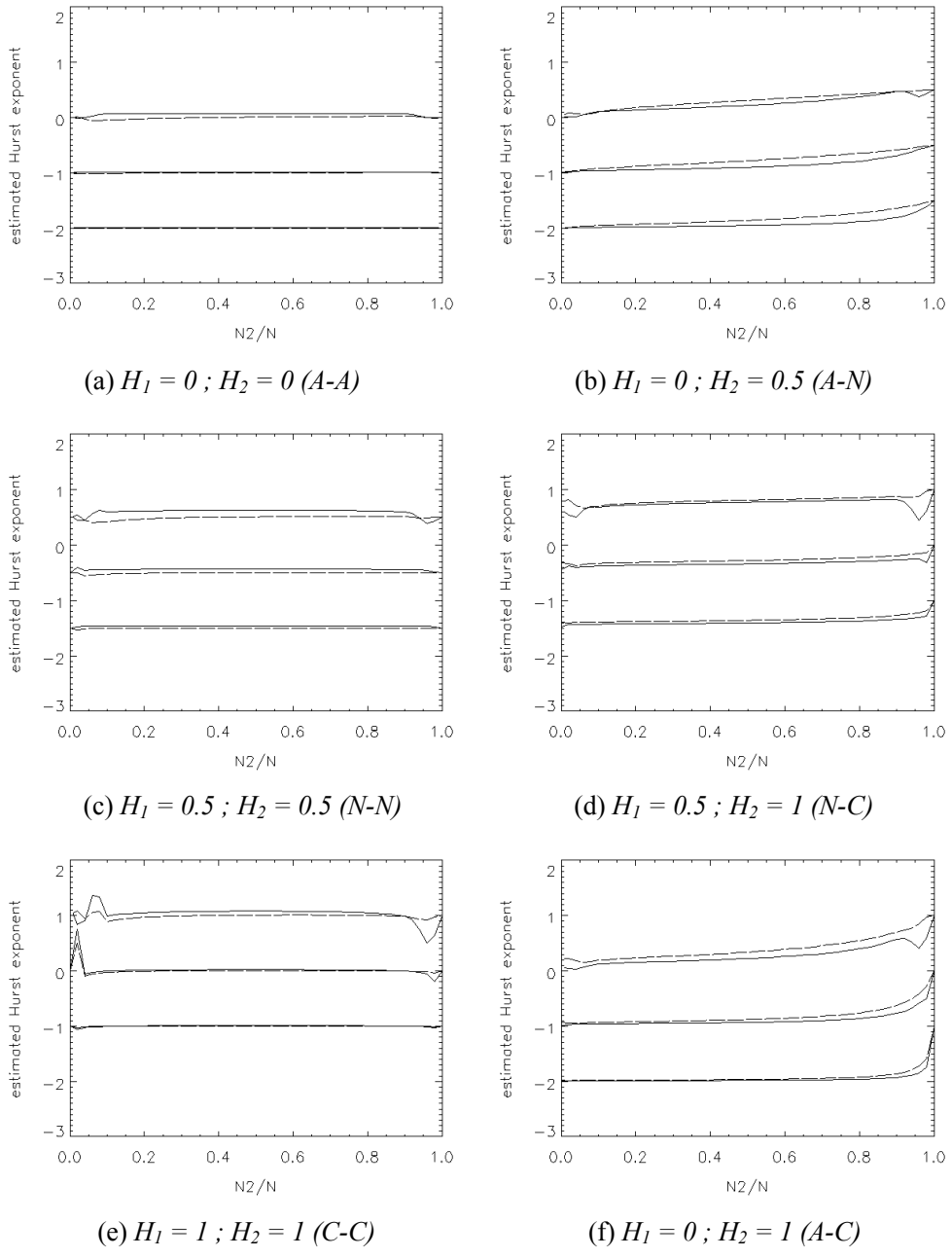

Fig. 10. Variations of the estimated fractal index H as a function of the relative structure size N_2/N in the μ, σ and detrended cases for monofractal (left) and bifractal (right) discontinuities. In each plot, N = 100, $N_1 = N_2$ = 50 (upper curves), N = 1000, $N_1 = N_2$ = 500 (middle curves) and N = 10 000, $N_1 = N_2$ = 5000 (lower curves); the middle and lower curves are shifted downwards by -1 and -2 respectively to avoid confusion. Same cases as Fig. 5.

b) an N-C case, consisting in two regions (H_1 = 1/2; H_2 = 1) with same (μ,σ);

c) an A-C case, consisting in two regions (H_1 = 0; H_2 = 1) with same (μ,σ).

In the monofractal cases (Figs. 10a, c, e), the discontinuity is due to a gap of μ or σ. The absence of oscillations enables a much better retrieval of the true behaviour and detrending the data does not make any difference if $\mu_1 = \mu_2$ (dotted and dashed lines coincide). Of course, the presence of the term proportional to $(\mu_1 - \mu_2)^2$ under the square root enhances some discrepancies at the segment boundaries (Fig. 10c, upper curves, solid line) and produces an overestimation in general, but these effects are smoothed as N increases (ibid. lower curves).

In the purely bifractal cases, the discontinuity is due to a gap of H (Figs. 10b, d, f). The monotonous increase of the function $H(H_2)$ is well verified, except for small irregularities at the segment boundaries too, in the vicinity of N_2 = 0

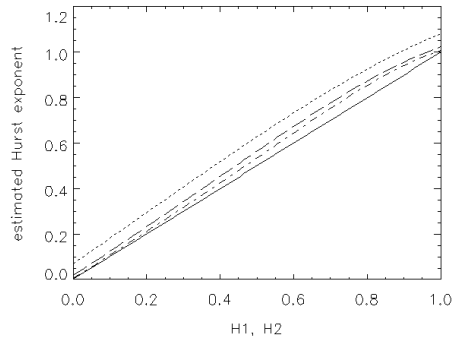

(a) $\mu_1 = 5$; $\mu_2 = 10$; $\sigma_1 = 1$; $\sigma_2 = 1$

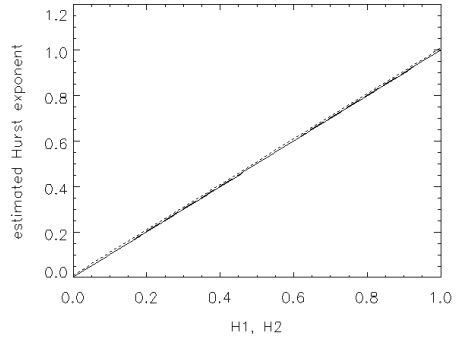

(b) $\mu_1 = 10$; $\mu_2 = 10$; $\sigma_1 = 1$; $\sigma_2 = 5$

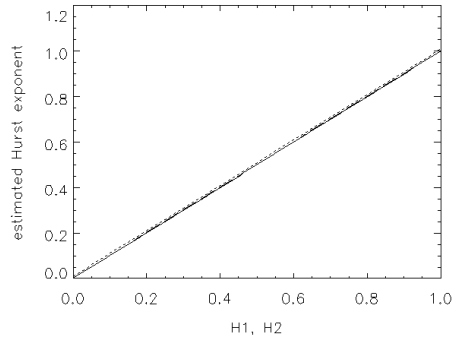

(c) $\mu_1 = 0$; $\mu_2 = 0$; $\sigma_1 = 1$; $\sigma_2 = 5$

Fig. 11. Variations of the estimated fractal index H as a function of the fractal index $H_1 = H_2$ (monofractal discontinuity) for raw **(a), (b)** and detrended **(c)** data. In each plot, N = 100, $N_1 = N_2$ = 50 (dotted line), N = 1000, $N_1 = N_2$ = 500 (dashed line), N = 10 000, $N_1 = N_2$ = 5000 (dotted-dashed line) and diagonal $H = H_1$ (solid line). Same cases as Fig. 6.

and $N_2 = N$ for small N (N = 100, 1000) due to sampling effects, which tend to vanish for larger N (N = 10 000, lower curves). Note that in this latter case the well-behaved profiles are highly non-linear and quickly increase near $N_2 = N$. This behaviour is quite similar to that of the spectral index (Figs. 5b, d, f).

For a monofractal discontinuity, the influence of (H_1, H_2) such that $H_1 = H_2$ is also investigated with $N_1 = N_2 = N/2$ (Fig. 11). It shows the retrieved parameter H_{est} to differ a little in excess from the theoretical value H when $\mu_1 \neq \mu_2$ (Fig. 11a), with $\Delta H = 0.05$ (N = 10 000) up to $\Delta H = 0.15$ (N = 100), but to get very close to H as σ/μ increases (Figs. 11b, c) whatever be H between 0 and 1. Moreover, as could be expected, the behaviour is exactly the same for detrended data (μ = 0; Fig. 11c) or for raw data without μ-gap ($\mu_1 = \mu_2$; Fig. 11b), and there is nearly no difference between estimated and original value. This again confirms published results already mentioned (Chen et al., 2002). Other authors (Schmittbuhl et al., 1995) found that small self-affine exponents are overestimated whereas large exponents are underestimated, which is rather the behaviour we found ourselves with the spectral method (Figs. 6a, b).

For a bifractal discontinuity, the influence of H_2 when H_1 is kept constant is investigated with $N_1 = N_2 = N/2$ (Fig. 12). It appears that the anti-correlated fluctuations (H_1 = 0) are predominant and cancel out the influence of the correlated fluctuations (Figs. 12a, b). The estimation is improved when the first medium is subject to correlated fluctuations (Fig. 12c). This is in agreement with already quoted works (Chen et al., 2002) which show that the behaviour of $\overline{\sigma}(L)$ is dominated by H_1 at small scales and H_2 at large scales when $H_1 < H_2$. There is again a slight overestimation of ΔH amounting 0.05 (N = 10 000) up to 0.15 (N = 100).

4 Consistency of both approaches

As relation (6) suggests, we may try to a certain extent to connect in our context (E=1) the behaviours of the spectral index β and the Hurst exponent H to check the consistency of both approaches.

A first difficulty arises because of the oscillations in the spectra, but this input is necessary because the gap of average levels (trends) is an important component of the discontinuity. A second problem is due to the property that the fractal model actually depends on two normalised parameters r_1 and r_2 through (30), whereas the spectral model depends on the four original parameters μ_1, μ_2, σ_1 and σ_2.

In connection with these features, from the $\beta(\beta_2)$ and $H(H_2)$ plots (Figs. 6 and 11, respectively) we can expect good consistency in the anti-correlation range ($1 < \beta < 2$ and $0 < H < 1/2$) and some saturation effects in the correlation range ($2 < \beta < 3$ and $1/2 < H < 1$). We choose the input β_1 and β_2 as equal to $2H_1$+1 and $2H_2$+1 so that we can check whether the output (β, H) is such that $\beta = 2H$+1, for a monofractal (Fig. 13) and a bifractal (Fig. 14) discontinuity.

For a monofractal discontinuity, relation (6) is exactly satisfied when data is trend-corrected (Fig. 13c). Otherwise, approximate linearity with $\beta > 2H + 1$ holds in the anti-correlation range and saturation takes place at $\beta \approx 2$ in the correlation range. The μ-gap (Fig. 13a) produces a larger deviation $|2H + 1 - \beta|$ than the σ-gap (Fig. 13b). This deviation vanishes in the vicinity of the correlation point (H = 1/2). The sample number N has little influence on the general behaviour and the saturation.

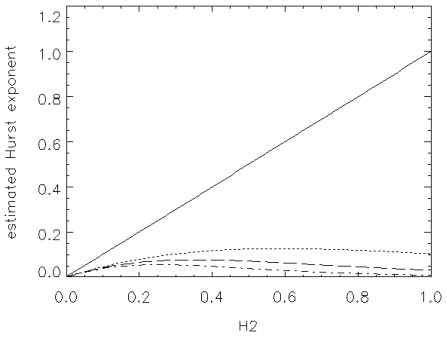

(a) $\mu_1 = 5$; $\mu_2 = 5$; $\sigma_1 = 1$; $\sigma_2 = 1$; $H_1 = 0$

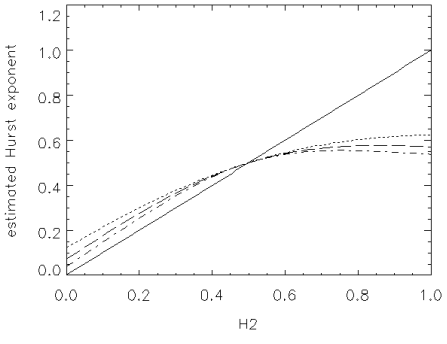

(b) $\mu_1 = 5$; $\mu_2 = 5$; $\sigma_1 = 1$; $\sigma_2 = 1$; $H_1 = 0.5$

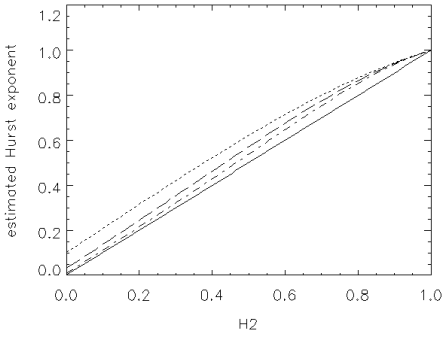

(c) $\mu_1 = 5$; $\mu_2 = 5$; $\sigma_1 = 1$; $\sigma_2 = 1$; $H_1 = 1$

Fig. 12. Variations of the estimated fractal index H as a function of the fractal index H_2 without μ or σ gap (bifractal discontinuity). In each plot, N = 100, $N_1 = N_2$ = 50 (dotted line), N = 1000, $N_1 = N_2$ = 500 (dashed line), N = 10 000, $N_1 = N_2$ = 5000 (dotted-dashed line) and diagonal $H = H_1$ (solid line). Same cases as Fig. 7.

For a bifractal discontinuity, the saturation has the effect of cutting off the curve part $H > H_1$, $\beta > \beta_1$. Raw data show relation (6) to be roughly satisfied in the anti-correlation range with a slight overestimation of β (Fig. 14, left side). Despite the cut-off, detrended data provide a better verification of relation (6), with a small underestimation of β, and the best agreement is obtained at $H_1 = H_2$ and $\beta_1 = \beta_2$ (Fig. 14, right side).

A somewhat similar comparison of two methods (rescaled-range and spectral analyses) has been carried out for a homogeneous medium subject to a pure FGN and several other kinds of processes (Rangarajan and Ding, 2000). This work shows that one of the two methods fails as soon as the underlying process is not fundamental and therefore relation (7) is not satisfied. For the standard analysis methods, relations (6) and (7) have been shown to work with Gaussian processes but to fail with log-normal processes (Malamud and Turcotte, 1999).

The influence of nonstationarities on the parameter retrieval by pure DFA has been addressed (Chen et al., 2000) in a more complex situation for a medium or signal composed of patches of two kinds randomly distributed whereas we consider only two such patches. Moreover, DFA requires a local linear fit of data in intervals which may have an impact on the results. The superposition rule in this work misses the term $\mu_1 - \mu_2$ due to the μ-gap and its influence.

5 Conclusion and prospects

The present paper has shown how much the structure of an inhomogeneous scalar field can influence the measurement of its own texture. The original model of discontinuity in a fractal field presented here has the advantage of not needing any calculation of a fractal field using a particular algorithm (multiplicative cascades, Weierstrass-Mandelbrot series, fractional integration of white noise…) or random functions, and it may pretend to some kind of universal characterisation. Nevertheless, this approach requires a careful calibration of the amplitude spectra (12) and the roughness function (21), which is a crucial step because it determines their precise dependence on the moments μ and σ.

This puts stress on the advantage of removing trends in data prior to processing, provided transitions and linear behaviour can be simply detected. If not, detrending may alter spectral slopes (Malamud and Turcotte, 1999). Moreover, the difficulty due to Fejer's kernel in estimating the slope of the side lobes is well known and has been addressed elsewhere (Rustom and Bélair, 1997).

Since we chose the outer scale wave number k_0 (or ξ_0 dimensionless) as inversely proportional to the total number of points N, we made its influence vanishing for large N. Nevertheless, for small samples, this parameter has a great importance: the media is no longer a pure fractal.

As for the fitting range, there is no definitive way to choose it, because it depends on the ratio μ/σ (Fig. 3). According to its value, the envelope of Fejer's kernel and the fractal spectrum cross at a specific abscissa k_i: in the range $k < k_i$, the latter contribution is higher, whilst in the range $k > k_i$, the former contribution is higher. The automatic detection of the best fitting intervals and crossovers has been addressed for geophysical data (Main et al., 1999), but for checking consistency with the fractal analysis in our analytical model it was simpler to take a compromise in a first step.

The parametric study performed here shows that for a pure μ-gap, H is well estimated everywhere though overestimated ($\Delta H \leq 0.15$) and β is overestimated in the anti-correlation range ($\Delta\beta \leq 0.7$) and saturates in the correlation range ($\beta \leq 2.5$). For a pure σ-gap the retrieval of H is excellent everywhere ($\Delta H \leq 0.01$) and the behaviour of β is better than for a μ-gap, leading to less overestimation in the anti-correlation range ($\Delta\beta \leq 0.2$). For detrended data H and β are well estimated everywhere. For a β-gap, saturation degrades measurements in the case of raw data and the medium with smaller spectral index is dominant in the case of detrended data. For a H-gap, there is also predominance of the medium with smaller fractal exponent. A similar comparison carried out with 50 realisations of a FGN (Taqqu et al., 1995) shows that the nominal value of H is retrieved within 1% to 10% accuracy, depending on the method used, but unfortunately, the problem of discontinuities is not addressed.

An interesting development of our one-dimensional model would be to insert a finite-gradient transition between the regions 1 and 2 (Fig. 14) so as to model a smoothed discontinuity. The signal function in the transition medium 0 would be locally split into an average μ_0 and a fluctuation with zero mean and standard deviation σ_0 like in Eq. (11). If this transition is composed of N_0 points, it can be assumed that μ_0 and σ_0 vary linearly in the intervals $[\mu_1,\mu_2]$ and $[\sigma_1,\sigma_2]$, respectively:

$$\begin{cases} \mu_0(x) = \frac{\mu_2-\mu_1}{N_0-1}x + \mu_1 \\ \sigma_0(x) = \frac{\sigma_2-\sigma_1}{N_0-1}x + \sigma_1 \end{cases} \quad 0 \leq x \leq N_0 - 1. \tag{31}$$

This kind of profile would be quite relevant since it would involve typical data segments from which linear trends are removed in the DFA method.

We actually focused here on the monofractal description of a bifractal object, because of our final purpose being the inverse problem of 2D- or 3D-synthesis from a minimal set of parameters. So to say, the present work basically considers a bifractal structure and examines the behaviour of the global structure seen as a monofractal.

Multifractals seem to be more realistic for modelling the texture of satellite images (Parrinello and Vaughan, 2002), the cloud liquid water content (Ivanova and Ackerman, 1999) and the dynamics of atmospheric phenomena (Schertzer and Lovejoy, 1988; Chigirinskaya et al., 1994; Lazarev et al., 1994). Nevertheless, the factors affecting multiscaling analysis (Harris et al., 1997) and the distinction between genuine and spurious multifractals have been also examined (Eneva, 1994; Tchiguirinskaia et al., 2000). Moreover, multifractal generation would require much more descriptive parameters (Tessier et al., 1993; Davis et al., 1994).

Because of this difficulty, the synthesis of multifractal data in two or three dimensions using a parametric process is not yet common, though very promising methods, based on wavelets (Deguy and Benassi, 2001), are presently gaining importance. In a multifractal analysis, instead of considering

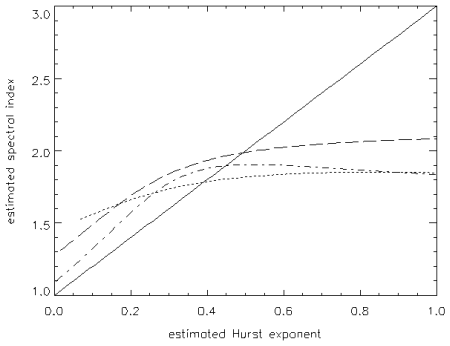

(a) $\mu_1 = 5$; $\mu_2 = 10$; $\sigma_1 = 1$; $\sigma_2 = 1$

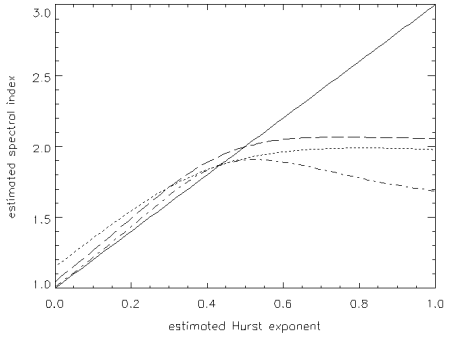

(b) $\mu_1 = 10$; $\mu_2 = 10$; $\sigma_1 = 1$; $\sigma_2 = 5$

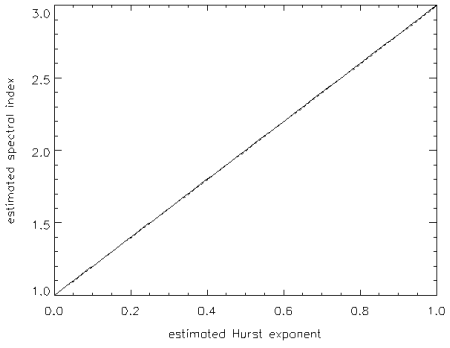

(c) $\mu_1 = 0$; $\mu_2 = 0$; $\sigma_1 = 1$; $\sigma_2 = 5$

Fig. 13. Consistency of the spectral and fractal approaches (monofractal discontinuity) for raw **(a), (b)** and detrended **(c)** data. In each plot, N = 100, N_1 = N_2 = 50 (dotted line), N = 1000, N_1 = N_2 = 500 (dashed line), N = 10 000, N_1 = N_2 = 5000 (dotted-dashed line) and diagonal $\beta = 2H + 1$ (solid line).

only the standard deviation σ such as expression (19), one has to involve the p-th order moments defined by:

$$m_p = \overline{(F-\mu)^p} \tag{32}$$

and such that:

$$\overline{m_p}\,(L) = m_0 \left(\frac{L}{L_0}\right)^{K(p)}, \tag{33}$$

where $K(p)$ is the moment scaling function (Tessier et al., 1993):

$$K(p) = pH(p). \tag{34}$$

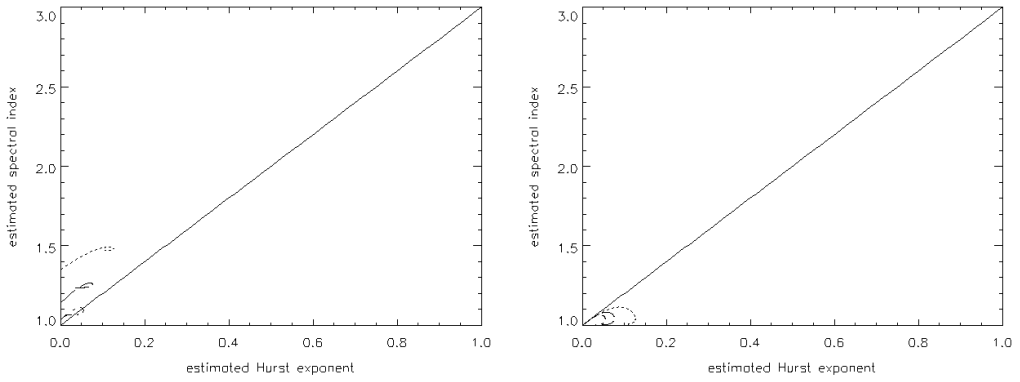

(a) $\mu_1 = 5$; $\mu_2 = 5$; $\sigma_1 = 1$; $\sigma_2 = 1$; $H_1 = 0$; $\beta_1 = 1$

(b) $\mu_1 = 0$; $\mu_2 = 0$; $\sigma_1 = 1$; $\sigma_2 = 1$; $H_1 = 0$; $\beta_1 = 1$

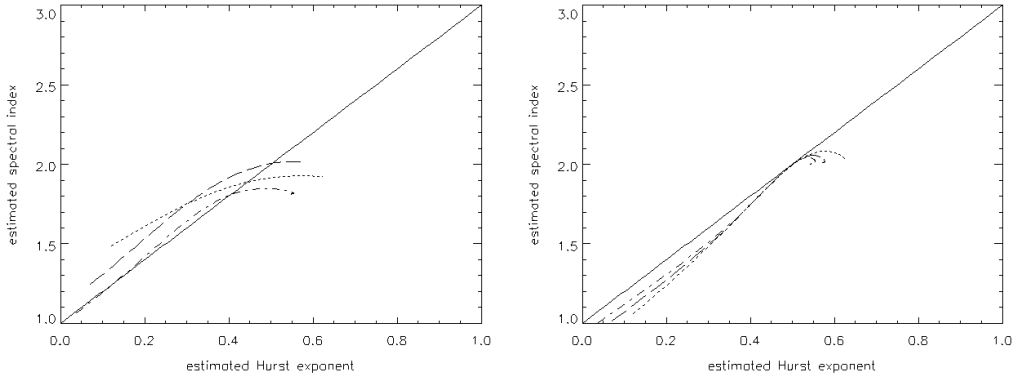

(c) $\mu_1 = 5$; $\mu_2 = 5$; $\sigma_1 = 1$; $\sigma_2 = 1$; $H_1 = 0.5$; $\beta_1 = 2$

(d) $\mu_1 = 0$; $\mu_2 = 0$; $\sigma_1 = 1$; $\sigma_2 = 1$; $H_1 = 0.5$; $\beta_1 = 2$

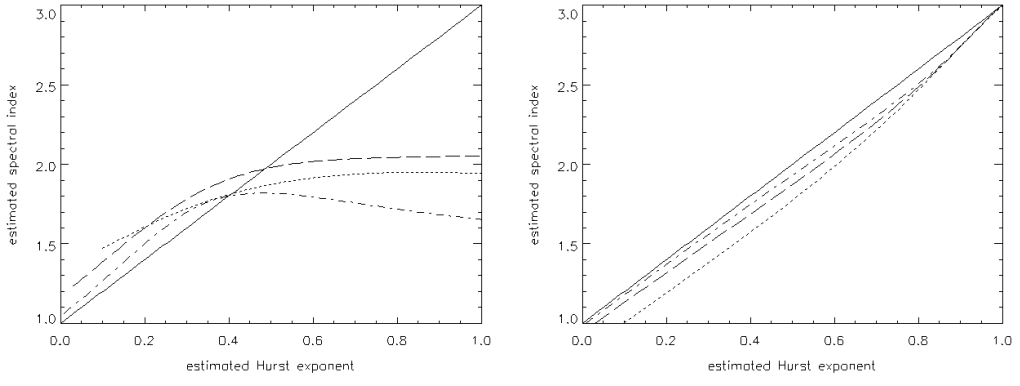

(e) $\mu_1 = 5$; $\mu_2 = 5$; $\sigma_1 = 1$; $\sigma_2 = 1$; $H_1 = 1$; $\beta_1 = 3$

(f) $\mu_1 = 0$; $\mu_2 = 0$; $\sigma_1 = 1$; $\sigma_2 = 1$; $H_1 = 1$; $\beta_1 = 3$

Fig. 14. Consistency of the spectral and fractal approaches (bifractal discontinuity) for raw (left) and detrended (right) data. In each plot, $N = 100$, $N_1 = N_2 = 50$ (dotted line), $N = 1000$, $N_1 = N_2 = 500$ (dashed line), $N = 10\,000$, $N_1 = N_2 = 5000$ (dotted-dashed line) and diagonal $\beta = 2H + 1$ (solid line).

For a monofractal $H(p)$ is a constant, independent of the order p. This development would therefore consist in extending the derivation of App. A2 to the moments of higher order.

The standpoint of monofractals has two advantages. On the one side, they require very few parameters and they are less complex for generating a large amount of 2D- or 3D-data in a short time, which is our very purpose. On the other side, we may consider in the present work the modelling of the first and second moments as a first step in the study of multifractal fields; the next steps would consist in modelling the moments of higher order (Eq. 33) in the same way.

Even in the frame of monofractals, the present model is based only on the estimation of the roughness parameter H. Nevertheless, it is well-known that a fractal structure must be characterised by its lacunarity, for which unfortunately only partial estimators exist (Mandelbrot, 1982; Allain and Cloitre, 1991; Albregtsen and Nielsen, 1995; Henebry and Kux, 1995; Plotnick et al., 1996). In other words a set with a given fractal dimension can be arranged to represent a broad range of quite different structures, differing only by their lacunarity (Blumenfeld and Mandelbrot, 1997). Actually the scaling relation (19) is subject to revision because the prefactor σ_0 is not necessarily a constant:

$$\overline{\sigma}(L) = \sigma_0(L)\left(\frac{L}{L_0}\right)^H. \tag{35}$$

Its variability has been proposed as a measure of lacunarity (Blumenfeld and Mandelbrot, 1997). We expect that these effects of lacunarity could be taken into account in a future work.

The confidence of Hurst parameter (Schmittbuhl et al., 1995), fractal dimension (Soille and Rivest, 1996) and spectral index (Malamud and Turcotte, 1999) measurements has been examined. It appears that the most robust methods to evaluate the fractal dimension are those of the semivariogram, the flat structuring element and the power spectrum. This latter one is based on the relationship between β and D derived by combination of relations (6) and (20):

$$\beta = 3E + 2 - 2D \tag{36}$$

with $E = 2$ in these authors' work and $E = 1$ in ours. Although the box counting method is less robust under linear transformation, in our context it is much easier to handle. Another extension to our work would consist in testing another method.

The one-dimensional approach of the problem proposed in this paper is basic because it naturally applies for instance to in situ measurements performed along the trajectory of an aircraft bearing instruments or to remote sensing of medium parameters along line scans performed by a lidar. Nevertheless, the extension to two-dimensional media would be interesting and necessary because we have also to analyse the texture of images.

Appendix A1: Power spectrum of a one-dimensional discontinuity

We wish to show the influence of a one-dimensional discontinuity between two monofractal regions on the Power-Spectral Density (PSD). In that purpose, we build here a one-dimensional model with a signal function $F(x)$. Let N_1, N_2 be the pixel number of regions 1 and 2 (and $N = N_1 + N_2$), μ_1, μ_2 their mean levels, σ_1, σ_2 their standard deviations and β_1, β_2 their spectral indices (Fig. 1).

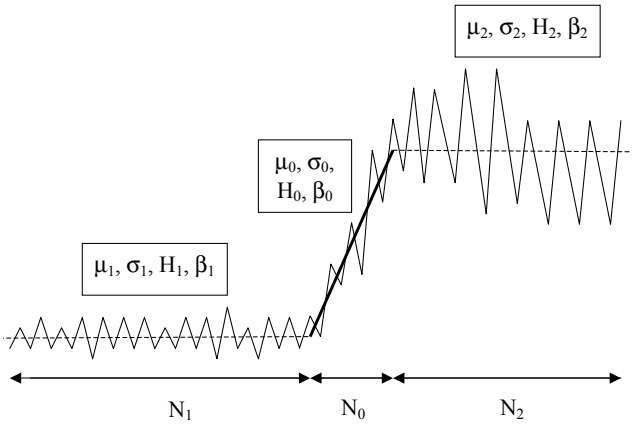

Fig. 15. Model of one-dimensional transition of finite gradient between two homogeneous fractal media.

We consider fields decomposed in two parts as defined by expression (11):

$$\begin{cases} F_1(x) = \mu_1 + G_1(x) \\ F_2(x) = \mu_2 + G_2(x) \end{cases} \tag{A1}$$

with

$$\begin{cases} \overline{G_1(x)} = 0 \\ \overline{G_2(x)} = 0 \end{cases} \qquad \begin{cases} \overline{G_1(x)^2} = \sigma_1^2 \\ \overline{G_2(x)^2} = \sigma_2^2 \end{cases}. \tag{A2}$$

The continuous Fourier transform of F on unbounded support writes:

$$\tilde{F}(k) = \mu_1\delta(k) + A_1(k)\,e^{i\Phi_1(k)} + \mu_2\delta(k) + A_2(k)\,e^{i\Phi_2(k)} \tag{A3}$$

with $\delta(k)$ denoting Dirac impulse, $\Phi_1(k)$, $\Phi_2(k)$ the phase spectra and $A_1(k)$, $A_2(k)$ the amplitude spectra of G_1 and G_2, respectively such that:

$$A_1(k) = \frac{a_1}{\left(k_{01}^2 + k^2\right)^{\beta_1/4}} \quad A_2(k) = \frac{a_2}{\left(k_{02}^2 + k^2\right)^{\beta_2/4}}. \tag{A4}$$

Now let $F(x)$ be sampled with a step Δx on a bounded domain containing the initial N points. Its Fourier transform writes:

$$\tilde{F}(k) = \mu_1 S_1(k) + T_1(k) + \mu_2 S_2(k) + T_2(k) \tag{A5}$$

with the following expressions, according to Eq. (8):

$$S_1(k) = \sum_{m=1}^{N_1} e^{ikm\Delta x} \qquad S_2(k) = \sum_{m=N_1+1}^{N} e^{ikm\Delta x} \tag{A6}$$

and:

$$T_1(k) = \sum_{m=1}^{N_1} G_1(m\Delta x)e^{ikm\Delta x} \quad T_2(k) = \sum_{m=N_1+1}^{N} G_2(m\Delta x)e^{ikm\Delta x}. \tag{A7}$$

It is straightforward to calculate the geometrical progressions (Eq. A6) putting Dirichlet kernels into evidence:

$$S_1(k) = \frac{\sin\frac{N_1 k\Delta x}{2}}{\sin\frac{k\Delta x}{2}} e^{i\frac{N_1+1}{2}k\Delta x} \quad S_2(k) = \frac{\sin\frac{N_2 k\Delta x}{2}}{\sin\frac{k\Delta x}{2}} e^{i\left(N_1+\frac{N_2+1}{2}\right)k\Delta x}. \tag{A8}$$

The expressions (A7) can be expressed by means of A_1, A_2, Φ_1, Φ_2:

$$\begin{cases} G_1(x) = \frac{1}{2\pi} \int_{-\infty}^{+\infty} A_1(k)\, e^{i\Phi_1(k)} e^{-ikx}\, dk \\ G_2(x) = \frac{1}{2\pi} \int_{-\infty}^{+\infty} A_2(k)\, e^{i\Phi_2(k)} e^{-ikx}\, dk \end{cases} \tag{A9}$$

to yield:

$$\begin{cases} T_1(k) = \frac{1}{2\pi} \int_{-\infty}^{+\infty} A_1(k')\, e^{i\Phi_1(k')} S_1(k-k')dk' \\ T_2(k) = \frac{1}{2\pi} \int_{-\infty}^{+\infty} A_2(k')\, e^{i\Phi_2(k')} S_2(k-k')dk' \end{cases} \tag{A10}$$

This means that $T_1(k)$, $T_2(k)$ are equal to the convolution of the kernels $S_1(k)$, $S_2(k)$ and the spectra on infinite support. Since these exact expressions are difficult to handle, we shall make a simplification by assuming that, in the limit of large N_1 and N_2, the sums S_1, S_2 as kernels in Eq. (A10) will give:

$$\begin{cases} S_1(k) \underset{N_1\to\infty}{\approx} 2\pi\ \delta(k)\ e^{i\frac{N_1+1}{2}k\Delta x} \\ S_2(k) \underset{N_2\to\infty}{\approx} 2\pi\ \delta(k)\ e^{i\left(N_1+\frac{N_2+1}{2}\right)k\Delta x} \end{cases} \tag{A11}$$

and therefore Eq. (A10) will reduce to:

$$T_1(k) \approx A_1(k) e^{i\Phi_1(k)} \qquad T_2(k) \approx A_2(k) e^{i\Phi_2(k)}. \tag{A12}$$

On the opposite, the sums S_1, S_2 as factors of μ_1, μ_2 in Eq. (A5) will be kept since they spread power over all scales. With Dirac impulse function in Eq. (A3) the continuum power would be concentrated at the origin ($k = 0$) so that it would not appear in log-log plots. In summary, inserting Eq. (A12) into Eq. (A5) we get:

$$\tilde{F}(k) = \mu_1 S_1(k) + A_1(k)\, e^{i\Phi_1(k)} + \mu_2 S_2(k) + A_2(k)\, e^{i\Phi_2(k)}. \tag{A13}$$

Let us now define the reduced wave number:

$$\xi = k\Delta x \tag{A14}$$

the sampling step Δk (dimensionless $\Delta\xi$) and the cut-off wave number k_N (dimensionless ξ_N):

$$\Delta k = \frac{\pi}{N\Delta x} \quad \Delta\xi = \frac{\pi}{N} \quad k_N = \frac{\pi}{\Delta x} \quad \xi_N = \pi. \tag{A15}$$

In Eq. (A4), the outer scale wave numbers k_{01}, k_{02} (dimensionless ξ_{01}, ξ_{02}) are defined as:

$$k_{01} = \frac{2\pi}{N\Delta x} \quad k_{02} = \frac{2\pi}{N\Delta x} \quad \xi_{01} = \frac{2\pi}{N} \quad \xi_{02} = \frac{2\pi}{N}. \tag{A16}$$

Thanks to Rayleigh's energy principle (equivalent to Parseval's theorem for continuous Fourier transform) which states that for any function F sampled at N points we have:

$$\sum_{m=1}^{N} F(x_m)^2 = \frac{1}{N} \sum_{n=1}^{N} \left|\tilde{F}(k_n)\right|^2 \tag{A17}$$

the variances of G_1 and G_2 can be easily expressed by means of their Fourier transforms:

$$\sigma_j^2 = \frac{1}{N_j} \sum_{m=1}^{N_j} G_j(x_m)^2 = \frac{1}{N_j^2} \sum_{n=1}^{N_j} A_j(k_n)^2 \tag{A18}$$

and yield the normalising constants of the amplitude spectra $A_1(k)$ and $A_2(k)$:

$$a_j = \frac{N_j}{\sqrt{J(N_j, \xi_{0j}, \beta_j)}}\sigma_j \qquad j \in \{1, 2\} \tag{A19}$$

with the sums:

$$J\left(N_j, \xi_{0j}, \beta_j\right) = \sum_{n=0}^{N_j} \frac{1}{\left(\xi_{0j}^2 + \xi_n^2\right)^{\beta_j/2}} \text{ where } \xi_n = \frac{n}{N}\xi_N. \tag{A20}$$

By taking the squared modulus of expression (A13) we get the PSD:

$$\begin{aligned} \left|\tilde{F}(k)\right|^2 =& \mu_1^2 |S_1(k)|^2 + \mu_2^2 |S_2(k)|^2 + A_1(k)^2 + A_2(k)^2 \\ &+ \mu_1\mu_2 \left[S_1(k)\, S_2(k)^* + S_1(k)^*\, S_2(k)\right] \\ &+ \mu_1 A_1(k) \left[S_1(k)\, e^{-i\Phi_1(k)} + S_1(k)^*\, e^{i\Phi_1(k)}\right] \\ &+ \mu_2 A_2(k) \left[S_2(k)\, e^{-i\Phi_2(k)} + S_2(k)^*\, e^{i\Phi_2(k)}\right] \\ &+ \mu_1 A_2(k) \left[S_1(k)\, e^{-i\Phi_2(k)} + S_1(k)^*\, e^{i\Phi_2(k)}\right] \\ &+ \mu_2 A_1(k) \left[S_2(k)\, e^{-i\Phi_1(k)} + S_2(k)^*\, e^{i\Phi_1(k)}\right] \\ &+ 2A_1(k)\, A_2(k) \cos\left[\Phi_1(k) - \Phi_2(k)\right]. \end{aligned} \tag{A21}$$

On the one hand, we shall focus on the phase-independent part of the PSD, and take the phase average of Eq. (A21), assuming uniformly-distributed random phases. This ensures that the quantities between the second, third, fourth and fifth brackets vanish. Moreover, if we assume that the two phase sets $\Phi_1(k)$ and $\Phi_2(k)$ are independent, the relevant terms (sixth brackets) also vanish, and there remains only:

$$\begin{aligned} \left|\tilde{F}(k)\right|^2 =& \mu_1^2 |S_1(k)|^2 + \mu_2^2 |S_2(k)|^2 + A_1(k)^2 \\ &+ A_2(k)^2 + \mu_1\mu_2 \left[S_1(k)\, S_2(k)^* + S_1(k)^*\, S_2(k)\right]. \end{aligned} \tag{A22}$$

On the other hand, taking ξ as the variable, we easily derive the expressions:

$$\begin{cases} |S_1(\xi)|^2 = \frac{\sin^2\frac{N_1\xi}{2}}{\sin^2\frac{\xi}{2}} \qquad |S_2(\xi)|^2 = \frac{\sin^2\frac{N_2\xi}{2}}{\sin^2\frac{\xi}{2}} \\ S_1(\xi)\, S_2(\xi)^* + S_1(\xi)^*\, S_2(\xi) = \frac{\cos N_1\xi + \cos N_2\xi - \cos N\xi - 1}{1-\cos\xi} \end{cases}, \tag{A23}$$

where we made use of the relation $N = N_1 + N_2$. Therefore, we get the simple expression for the PSD:

$$\begin{aligned} \left|\tilde{F}(\xi)\right|^2 =& \frac{(\mu_1-\mu_2)\left(\mu_1 \sin^2\frac{N_1\xi}{2} - \mu_2 \sin^2\frac{N_2\xi}{2}\right) + \mu_1\mu_2 \sin^2\frac{N\xi}{2}}{\sin^2\frac{\xi}{2}} \\ &+ \frac{N_1^2}{J_1} \frac{\sigma_1^2}{\left(\xi_{01}^2+\xi^2\right)^{1+\beta_1/2}} + \frac{N_2^2}{J_2} \frac{\sigma_2^2}{\left(\xi_{02}^2+\xi^2\right)^{1+\beta_2/2}} \end{aligned} \tag{A24}$$

that is, relation (15) in the main text. Note that the steady components are functions of Fejer's kernels relative to N, N_1

and N_2. In the limit of vanishing N_1 or N_2, relation (A24) reduces to:

$$\begin{cases} \left|\tilde{F}(\xi)\right|^2 \underset{N_1\to 0}{\propto} \mu_2^2 \frac{\sin^2\frac{N\xi}{2}}{\sin^2\frac{\xi}{2}} + \frac{N^2}{J_2}\frac{\sigma_2^2}{\left(\xi_{02}^2+\xi^2\right)^{1+\beta_2/2}} \\ \left|\tilde{F}(\xi)\right|^2 \underset{N_2\to 0}{\propto} \mu_1^2 \frac{\sin^2\frac{N\xi}{2}}{\sin^2\frac{\xi}{2}} + \frac{N^2}{J_1}\frac{\sigma_1^2}{\left(\xi_{01}^2+\xi^2\right)^{1+\beta_1/2}} \end{cases} \quad \text{(A25)}$$

The condition (A1) on the averages of G_1 and G_2 leads to:

$$A_1(0)e^{i\Phi_1(0)} = 0 \qquad A_2(0)e^{i\Phi_2(0)} = 0 \quad \text{(A26)}$$

and since $A_1(0) \neq 0$ and $A_2(0) \neq 0$, we conclude that:

$$\Phi_1(0) = \frac{\pi}{2}\,[\mathrm{mod}\pi] \qquad \Phi_2(0) = \frac{\pi}{2}\,[\mathrm{mod}\pi]\,. \quad \text{(A27)}$$

Appendix A2: Fractal roughness of a one-dimensional discontinuity

We want to demonstrate the influence of a one-dimensional discontinuity between two monofractal regions on the roughness parameter H. In that purpose, we build a one-dimensional model with a signal function $F(x)$. Let N_1, N_2 be the pixel number of regions 1 and 2, μ_1, μ_2 their mean levels, σ_1, σ_2 their standard deviations and H_1, H_2 their Hurst parameters (Fig. 1). We shall use the box-counting method, by counting the positions of a box with normalised size L which yield the same standard deviation $\sigma(L)$. Three main cases and two trivial cases can be distinguished.

1) if $0 \leq L \leq \min(N_1, N_2)$, three situations are possible. There are $N_1 + 1 - L$ box positions where:

$$\begin{cases} \mu = \mu_1 \\ \sigma = \sigma_1 \left(\frac{L}{N_1}\right)^{H_1} \end{cases} \quad \text{(A28)}$$

and $N_2 + 1 - L$ positions where:

$$\begin{cases} \mu = \mu_2 \\ \sigma = \sigma_2 \left(\frac{L}{N_2}\right)^{H_2} \end{cases} \quad \text{(A29)}$$

since the structures 1 and 2 are assumed to be fractal. Besides, there are also $L - 1$ box positions in which:

$$\begin{cases} \mu = \alpha\overline{F_1} + (1-\alpha)\overline{F_2} \\ \sigma^2 = \alpha\overline{(F_1-\mu)^2} + (1-\alpha)\overline{(F_2-\mu)^2} \end{cases}, \quad \text{(A30)}$$

where α represents the fraction of region 1 covered by the box, such that:

$$\alpha = \frac{n}{L} \quad \text{with} \quad 1 \leq n \leq L-1. \quad \text{(A31)}$$

Replacing μ by its expression, we get:

$$\begin{cases} F_1 - \mu = F_1 - \mu_1 + (1-\alpha)(\mu_1 - \mu_2) \\ F_2 - \mu = F_2 - \mu_2 - \alpha(\mu_1 - \mu_2) \end{cases} \quad \text{(A32)}$$

and therefore, taking the square and the average:

$$\begin{cases} \overline{(F_1-\mu)^2} = \overline{(F_1-\mu_1)^2} + (1-\alpha)^2(\mu_1-\mu_2)^2 \\ \overline{(F_2-\mu)^2} = \overline{(F_2-\mu_2)^2} + \alpha^2(\mu_1-\mu_2)^2 \end{cases}. \quad \text{(A33)}$$

Since the regions 1 and 2 are fractal, we have:

$$\begin{cases} \overline{(F_1-\mu_1)^2} = \sigma_1^2 L^{2H_1} \\ \overline{(F_2-\mu_2)^2} = \sigma_2^2 L^{2H_2} \end{cases} \quad \text{(A34)}$$

and by inserting Eqs. (A33) and (A34) into Eq. (A30) we get:

$$\begin{cases} \mu = \alpha\mu_1 + (1-\alpha)\mu_2 \\ \sigma^2 = \alpha\sigma_1^2 L^{2H_1} + (1-\alpha)\sigma_2^2 L^{2H_2} + \alpha(1-\alpha)(\mu_1-\mu_2)^2 \end{cases}. \quad \text{(A35)}$$

We can check that the total number of the positions equals $(N_1+1-L) + (N_2+1-L) + (L-1) = N - L + 1$ where we have set $N=N_1+N_2$. By weighting each value of σ by its frequency of occurrence, we eventually get the average:

$$(N-L+1)\overline{\sigma}(L) = \sum_{n=1}^{L-1}\sqrt{\frac{n}{L}\sigma_1^2\left(\frac{L}{N_1}\right)^{2H_1} + \left(1-\frac{n}{L}\right)\sigma_2^2\left(\frac{L}{N_2}\right)^{2H_2} + \frac{n}{L}\left(1-\frac{n}{L}\right)(\mu_1-\mu_2)^2} + \sigma_1(N_1+1-L)\left(\frac{L}{N_1}\right)^{H_1} + \sigma_2(N_2+1-L)\left(\frac{L}{N_2}\right)^{H_2} \quad \text{(A36)}$$

that is, relation (22) in the main text.

2) if $\max(N_1, N_2) \leq L \leq N$, only one situation is possible. We find $N_1+N_2-L+1 = N-L+1$ box positions where relations (A30) hold with α representing the covering fraction of region 1 defined by Eq. (A31). After a calculation similar to that of the previous case, we likewise derive relations (A35). Like previously the total number of the positions equals $N-L+1$ ($N = N_1+N_2$). By weighting each value of σ by its frequency of occurrence, we finally get the average:

$$(N-L+1)\overline{\sigma}(L) = \sum_{n=1}^{N-L+1}\sqrt{\frac{n}{L}\sigma_1^2\left(\frac{L}{N_1}\right)^{2H_1} + \left(1-\frac{n}{L}\right)\sigma_2^2\left(\frac{L}{N_2}\right)^{2H_2} + \frac{n}{L}\left(1-\frac{n}{L}\right)(\mu_1-\mu_2)^2} \quad \text{(A37)}$$

that is, relation (23) in the main text.

3) if $\min(N_1, N_2) \leq L \leq \max(N_1, N_2)$, two sub-cases are possible, according to whether $N_1 < N_2$ or $N_2 < N_1$. If $N_1 < N_2$, we find N_1 box positions where relations (A30) hold with α representing the covering fraction of region 1 defined by (A31), and $N_2 + 1 - L$ positions where relations (A29) hold. After a calculation similar to that of the first case, we likewise derive relations (A35). We can check again that the total number of the positions equals $(N_1) + (N_2+1-L) = N-L+1$. By weighting each value of σ by its frequency of occurrence, we finally get the average:

$$(N-L+1)\overline{\sigma}(L) = \sum_{n=1}^{N_1}\sqrt{\frac{n}{L}\sigma_1^2\left(\frac{L}{N_1}\right)^{2H_1} + \left(1-\frac{n}{L}\right)\sigma_2^2\left(\frac{L}{N_2}\right)^{2H_2} + \frac{n}{L}\left(1-\frac{n}{L}\right)(\mu_1-\mu_2)^2} + \sigma_2(N_2+1-L)\left(\frac{L}{N_2}\right)^{H_2} \quad \text{(A38)}$$

that is, relation (24) in the main text.

If $N_2 < N_1$, we find N_2 box positions where relations (A30) hold with α representing the covering fraction of region 1 defined by Eq. (A31), and N_1+1-L positions where relations (A28) hold. After a calculation similar to that of the first case, we likewise derive relations (A35). We can check that the total number of the positions equals $(N_1 + 1 - L) + (N_2) = N - L + 1$. By weighting each value of σ by its frequency of occurrence ($N = N_1 + N_2$), we finally get the average:

$$(N-L+1)\overline{\sigma}(L) = \sum_{n=1}^{N_2}\sqrt{\frac{n}{L}\sigma_1^2\left(\frac{L}{N_1}\right)^{2H_1} + \left(1-\frac{n}{L}\right)\sigma_2^2\left(\frac{L}{N_2}\right)^{2H_2} + \frac{n}{L}\left(1-\frac{n}{L}\right)(\mu_1-\mu_2)^2} + \sigma_1(N_1+1-L)\left(\frac{L}{N_1}\right)^{H_1} \quad \text{(A39)}$$

that is, relation (25) in the main text.

Eventually, the two trivial cases $N_1 = 0$ and $N_2 = 0$ lead to dropping the square root sums in Eqs. (A38) and (A39) to yield respectively

$$\text{if } N_1 = 0: \qquad \overline{\sigma}(L) = \sigma_2\left(\frac{L}{N}\right)^{H_2} \quad \text{(A40)}$$

$$\text{if } N_2 = 0: \qquad \overline{\sigma}(L) = \sigma_1\left(\frac{L}{N}\right)^{H_1} \quad \text{(A41)}$$

that is, relations (26) and (27) in the main text.

Appendix A3: Numerical generator of fractional Brownian motion (FBM)

To check the calibration of our analytic model, we generate a signal $F(x)$ of FBM type with spectral index β and equivalent Hurst parameter H given by Eq. (6) by integration of a Gaussian white noise $W(x)$ through the left-sided Riemann-Liouville integral (Mandelbrot and Van Ness, 1968):

$$F(x) - F(0) = \frac{1}{\Gamma(H+1/2)} \left\{ \int_{-\infty}^{0} \left[(x-u)^{H-1/2} - (-u)^{H-1/2}\right] W(u)du + \int_{0}^{x} (x-u)^{H-1/2} W(u)du \right\} \quad \text{(A42)}$$

then by a simple calibration ensuring that μ and σ will be the average and standard deviation of the resulting signal:

$$B = \sigma\frac{F-\bar{F}}{\sqrt{\overline{F^2}-\bar{F}^2}} + \mu \quad \text{(A43)}$$

and eventually perform Fourier transform through Eq. (8) or fractal analysis. Since our signal is limited to the finite set (0, N), we keep only the second integral, and of course convert it to a sampled sum:

$$F_n = \sum_{j=0}^{n} (n-j)^{H-1/2} W_j. \quad \text{(A44)}$$

We also dropped the integration constant $F(0)$, the normalising constant Γ(H+1/2) and the sampling step Δx because the calibration of relation (A43) normalises it again anyway. The sampled Gaussian white noise W_j is calculated by means of a random number generator.

Examples of spectra and fractal graphs of this numerical model are plotted on Figs. 3 and 8, together with the analytical spectra and fractal graph possessing the same μ, σ, β, H. The agreement between both models seems quite satisfying, as regards levels and slopes. Nevertheless the retrieved slope is overestimated when $H < 1/2$, and this is probably due to the truncation in the series of relation (A44). Since this random FBM is aimed only at validating the calibration of our analytical spectrum, we shall ignore this discrepancy.

Acknowledgements. The author is grateful to the referees for valuable remarks, to the editor (B. D. Malamud) for advice, and especially to one of the referees for useful discussion and references. The efficient support of C. Appriou (ONERA Library) in providing some important reference papers is also thankfully acknowledged.

Edited by: B. D. Malamud
Reviewed by: 2 referees

References

Albregtsen, F. and Nielsen, B.: Fractal dimension and lacunarity estimated by sequential 1D polygonization of 2D images, 9th Scandinavian Conf. on Image Analysis, Uppsala, Sweden, June 1995, 575–582, 1995.

Allain, C. and Cloitre, M.: Characterizing the lacunarity of random and deterministic fractal sets, Phys. Rev. A, 44(6), 3552–3558, 1991.

Ausloos, M. and Berman, D. H.: A multivariate Weierstrass-Mandelbrot function, P. Roy. Soc. A, 400, 331–350, 1985.

Ausloos, M., Vandewalle, N., Boveroux, Ph., Minguet, A., and Ivanova, K.: Applications of statistical physics to economic and financial topics, Physica A, 274, 229–240, 1999.

Bachelier, E., Ruiz, C., Borderies, P., Chênerie, I., and Davidson, M.: Weierstrass functions determination for soil modeling, IGARSS-98 Int. Geoscience and Remote Sensing Symp., 6–10 July 1998.

Berizzi, F., Dalle Mese, E., and Pinelli, G.: A two-dimensional fractal model of the sea surface and sea spectrum evaluation, IEE Radar Conf. 97, 14–16 Oct. 1997, 189–193, 1997.

Berry, M. V. and Lewis, Z. V.: On the Weierstrass-Mandelbrot fractal function, P. Roy. Soc. A, 370, 459–484, 1980.

Blumenfeld, R. and Mandelbrot, B. B.: Lévy dusts, Mittag-Leffler statistics, mass fractal lacunarity, and perceived dimension, Phys. Rev. E, 56(1), 112–118, 1997.

Buczkowski, S., Kyriacos, S., Nekka, F., and Cartilier, L.: The modified box-counting method: analysis of some characteristic parameters, Patt. Recog., 11(4), 411–418, 1998.

Buldyrev, S. V., Goldberger, A. L., Havlin, S., Mantegna, R. N., Matsa, M. E., Peng, C.-K., Simons, M. and Stanley, H. E.: Long-range correlation properties of coding and noncoding DNA sequences: GenBank analysis, Phys. Rev. E, 51(5), 5084–5091, 1995.

Bulmer, M.: Music from fractal noise, Mathematics 2000 Festival, Melbourne, 10-13 January, 2000.

Cahalan, R. F.: Bounded cascade clouds: albedo and effective thickness, Nonl. Pr. Geo., 1, 156–167, 1994.

Carvalho, L. M. V. and Silva Dias, M. A. F.: An application of fractal box dimension to the recognition of mesoscale cloud patterns in infrared satellite images, J. App. Met., 37(10), 1265–1282, 1998.

Chen, J., Lo, T. K. Y., Leung, H., and Litva, J.: The use of fractals for modeling EM waves scatttering from rough sea surfaces, IEEE T. Geo. Remot. Sen., 34(4), 966–972, 1996.

Chen, Y., Ding, M., and Kelso, J. A. S.: Long memory processes ($1/f^{\alpha}$ type) in human coordination, Phys. Rev. L., 79(22), 4501–4504, 1997.

Chen, Z., Ivanov, P. Ch., Hu, K., and Stanley, H. E.: Effect of nonstationarities on detrended fluctuation analysis, Phys. Rev. E, 65, 041107, 1–15, 2002.

Chigirinskaya, Y., Schertzer, D., Lovejoy, S., Lazarev, A., and Ordanovich, A.: Unified multifractal atmospheric dynamics tested in the tropics : Part I. Horizontal scaling and self criticality, Nonl. Pr. Geo., 1, 105–114, 1994.

Cianciolo, M. E.: Cloud scene simulation for the Smart Weapons Operability Enhancement program, SPIE, 1967, 507–514, 1993.

Curran, P.J.: The semivariogram in remote sensing: an introduction, Remot. Sen. E., 24, 493–507, 1988.

Davis, A., Marshak, A., Wiscombe, W., and Cahalan, R.: Multifractal characterisations of nonstationarity and intermittency in geophysical fields : observed, retrieved or simulated, J. Geo. Res., 99(D4), 8055–8072, 1994.

Davis, A., Marshak, A., Wiscombe, W., and Cahalan, R.: Scale invariance of liquid water distributions in marine stratocumulus. Part I: spectral properties and stationary issues, J. Atmos. Sci., 53(11), 1538–1558, 1996.

De Cola, L.: Fractal analysis of a classified Landsat scene, Photogr. E. R., 55(5), 601–610, 1991.

Deguy, S. and Benassi, A.: A flexible noise model for designing maps, Vision, Modeling, and Visualization, Stuttgart, 21–23 Nov., 2001.

Domon, M. and Honda, E.: Correlation of measured fractal dimensions with lacunarities in computer-generated three-dimensional images of Cantor sets and those of fractional Brownian motion, Forma, 14, 249–263, 1999.

Echeverria, J. C., Woolfson, M. S., Crowe, J. A., Hayes-Gill, B. R., Croaker, G. D. H. and Vyas, H.: Interpretation of heart rate variability via detrended fluctuation analysis and $\alpha\beta$ filter, Chaos, 13(2), 467–475, 2003.

Elliott, R. N.: The wave principle, 1938.

Eneva, M.: Monofractal or multifractal: a case study of spatial distribution of mining induced seismic activity, Nonl. Pr. Geo., 1, 182–190, 1994.

Gammel, B. M.: Hurst's rescaled range statistical analysis for pseudorandom number generators used in physical simulations, Phys. Rev. E, 58(2), 2586–2597, 1998.

Geraets, W. G. M. and van der Stelt, P. F.: Fractal properties of bone, Dentromax. R., 29, 144–153, 2000.

Germann, U. and Joss, J.: Variograms of radar reflectivity to describe the spatial continuity of Alpine precipitation, J. App. Met., 40, 1042–1059, 2001.

Gneiting, T. and Schlather, M.: Stochastic models that separate fractal dimension and the Hurst effect, SIAM Rev., 46(2), 269–282, 2004.

Gotoh, K. and Fujii, Y. : A fractal dimensional analysis on the cloud shape parameters of cumulus over land, J. App. Met., 37(10), 1283–1292, 1998.

Hagerhall, C. M., Purcell, T., and Taylor, R.: Fractal dimension of landscape silhouette outlines as a predictor of landscape preference, J. Envir. Psy., 24, 247–255, 2004

Harris, D., Seed, A., Menabde, M., and Austin, G.: Factors affecting multiscaling analysis of rainfall time series, Nonl. Pr. Geo., 4, 137–155, 1997.

Henebry, G. M. and Kux, H. J. H.: Lacunarity as a texture measure for SAR imagery, Int. J. Remot. Sen., 16(3), 565–571, 1995.

Henegan, C. and Mc Darby, G.: Establishing the relation between detrended fluctuation analysis and power spectral density analysis for stochastic processes, Phys. Rev. E, 62(5), 6103–6110, 2000.

Hunt, B. R.: The Hausdorff dimension of graphs of Weierstrass functions, P. Am. Math. S., 126(3), 791–800, 1998.

Hurst, H. E.: Long-term storage capacity of reservoirs, T. Am. S. Civ. Eng., 116, 770–808, 1951.

Ivanov, P. Ch., Amaral, L. A. N., Goldberger, A. L., Havlin, S., Rosenblum, M. G., Stanley, H. E., and Struzik, Z. R.: From 1/f noise to multifractal cascades in heartbeat dynamics, Chaos, 11(3), 641–652, 2001.

Ivanova, K. and Ackerman, T.: Multifractal characterization of liquid water in clouds, Phys. Rev. E, 59(3), 2778–2782, 1999.

Ivanova, K. and Ausloos, M.: Application of the detrended fluctuation analysis (DFA) for describing cloud breaking, Physica A, 274, 349–354, 1999.

Ivanova, K., Ausloos, M., Davis, A. B., and Ackerman, T.P.: Atmospheric data analysis with the i-variability diagram method: hint to fractional Brownian motion-like phenomena for the inner structure of clouds, Physica A, 272, 269–277, 1999.

Ivanova, K., Shirer, H.N., Clothiaux, E.E., Kitova, N., Mikhalev, M. A., Ackerman, T. P., and Ausloos, M.: A case study of stratus cloud base height multifractal fluctuations, Physica A, 308, 518–532, 2002.

Ivanova, K., Ackerman, T. P., Clothiaux, E. E., Ivanov, P. Ch., Stanley, H. E. and Ausloos, M.: Time correlations and 1/f behavior in backscattering radar reflectivity measurements from cirrus cloud ice fluctuations, J. Geo. Res., 108(D9), AAC03, 2003.

Jennane, R., Harba, R., and Jacquet, G.: Synthèse précise d'images fractales, 16$^{\text{th}}$ GRETSI, 15–19 Sept. 1997, 487–490, 1997.

Kube, P. and Pentland, A.: On the imaging of fractal surfaces, IEEE Patt. A., 10(5), 704–707, 1988.

Labini, F. Sylos, Montuori, M., and Pietronero, L.: Scale-invariance of galaxy clustering, Phys. Report, 293(2-4), 61-226, 1998.

Lazarev, A., Schertzer, D., Lovejoy, S., and Chigirinskaya, Y.: Unified multifractal atmospheric dynamics tested in the tropics : Part II. Vertical scaling and generalized scale invariance, Nonl. Pr. Geo., 1, 115–123, 1994.

Lévesque, M. P.: Dynamic sea image generation, SPIE, Characterization, Propagation and Simulation of Sources and Backgrounds, 1486, 294–300, 1991.

Lovejoy, S.: Area-perimeter relation for rain and cloud areas, Science, 216, 185–187, 1982.

Main, I. G., Leonard, T., Papasouliotis, O., Hatton, C. G., and Meredith, P. G.: One slope or two? Detecting statistically significant breaks of slope in geophysical data, with application to frac-

ture scaling relationships, Geophys. R. L., 26(18), 2801–2804, 1999.

Malamud, B. D. and Turcotte D. L.: Self-affine time series: Generation and analysis, Advances in Geophysics, Academic Press, 40, 1–90, 1999.

Malinowski, S. P. and Zawadzki, I.: On the surface of clouds, J. Atmos. Sci., 50(1), 5–13, 1993.

Mallat, S.: A wavelet tour of signal processing, Academic Press, 1998.

Mandelbrot, B. B. : Intermittent turbulence in self-similar cascades: divergence of high moments and dimension of the carrier, J. Fluid Mech., 62, 331–358, 1974.

Mandelbrot, B. B.: The fractal geometry of nature, W. H. Freeman, San Francisco, 1982.

Mandelbrot, B. B.: Fractals and scaling in finance, Springer-Verlag, 1997.

Mandelbrot, B. B. and Van Ness, J. W.: Fractional Brownian motions, fractional noises and applications, SIAM Rev., 10(4), 422–437, 1968.

Menabde, M.: Bounded lognormal cascades as quasi-multiaffine random processes, Nonl. Pr. Geo., 5, 63–68, 1998.

Moghaddam, B., Hintz, K. J., and Stewart, C. V.: Dimension and lacunarity measurement of IR images using Hilbert scanning, SPIE, 1486, 115–126, 1991.

Parrinello, T. and Vaughan, R. A.: Multifractal analysis and feature extraction in satellite imagery, Int. J. Remot. Sen., 23(9), 1799–1825, 2002.

Peng, C.-K., Buldyrev, S. V., Havlin, S., Simons, M., Stanley, H. E., and Goldberger, A. L.: Mosaic organization of DNA nucleotides, Phys. Rev. E, 49(2), 1685–1689, 1994.

Plotnick, R. E., Gardner, R. H., Hargrove, W. W., Prestegaard, K., and Perlmutter, M.: Lacunarity analysis: A general technique for the analysis of spatial patterns, Phys. Rev. E, 53(5), 5461–5468, 1996.

Rangarajan, G. and Ding, M.: Integrated approach to the assessment of long range correlation in time series data, Phys. Rev. E, 61(5), 4991–5001, 2000.

Rustom, C. and Bélair, J.: Estimation numérique de la vitesse de décroissance des spectres de puissance, J. Phys. A, 30, 2197–2209, 1997.

Saupe, D.: Point evaluation of multi-variable random fractals, Visualisierung in Mathematik und Naturwissenschaften, Bremer Computergraphik-Tage, 1988.

Scafetta, N. and Grigolini, P.: Scaling detection in time series: diffusion entropy analysis, Phys. Rev. E, 66, 036130, 2002.

Scafetta, N., Hamilton, P., and Grigolini, P.: The thermodynamics of social processes: the teen birth phenomenon, Fractals, 9(2), 193–208, 2001.

Schertzer, D. and Lovejoy, S.: Multifractal simulations and analysis of clouds by multiplicative processes, Atmos. Res., 21, 337–361, 1988.

Schlesinger, M. F. and West, B. J.: Complex fractal model of the bronchial tree, Phys. Rev. L., 67(15), 2106–2108, 1991.

Schmittbuhl, J., Vilotte, J.-P., and Roux, S.: Reliability of self-affine measurements, Phys. Rev. E, 51(1), 131–147, 1995.

Scotti, A. and Meneveau, C.: A fractal model for large eddy simulation of turbulent flow, Physica D, 127, 198-232, 1999.

Simoneau, P., Berton, R., Caillault, K., Durand, G., Huet, T., Labarre, L., Malherbe, C., Miesch, C., Roblin, A., and Rosier, B.: MATISSE: Advanced Earth Modeling for Imaging and Scene Simulation, Int. Symp. OPTRO 2002, Paris, France, 14–16 January 2002.

Simonsen, I., Hansen, A., and Nes, O. M.: Determination of the Hurst exponent by use of wavelet transforms, Phys. Rev. E, 58(4), 2779–2787, 1998.

Soille, P. and Rivest, J.-F.: On the validity of fractal dimension measurements in image analysis, J. Vis. C. Im., 7(3), 217–229, 1996.

Southgate, H. N. and Möller, I.: Fractal properties of coastal profile evolution at Duck, North Carolina, J. Geo. Res., 105(C5), 11489–11507, 2000.

Spehar, B., Clifford, C. W. G., Newell, B. R., and Taylor, R. P.: Universal aesthetics of fractals, Comput. Grap., 27, 813–820, 2003.

Stutzki, J., Bensch, F., Heithausen, A., Ossenkopf, V. and Zielinsky, M.: On the fractal structure of molecular clouds, Astron. Astr., 336, 697–720, 1998.

Taqqu, M. S., Teverovsky, V., and Willinger, W.: Estimators for long-range dependence: an empirical study, Fractals, 3(4), 785–798, 1995.

Tchiguirinskaia, I., Lu, S., Molz, F. J., Williams, T. M., and Lavallée, D.: Multifractal versus monofractal analysis of wetland topography, Stoc. Env. R., 14, 8–32, 2000.

Tessendorf, J., Weston, D., and Taylor, L.: Structure of spatial spectra of simulated cloud scenes at infrared wavelengths, SPIE, 1687, 499–507, 1992.

Tessier, Y., Lovejoy, S., and Schertzer, D.: Universal multifractals: theory and observations for rain and clouds, J. App. Met., 32(2), 223–250, 1993.

Theiler, J.: Estimating fractal dimension, J. Opt. Soc. A., 7(6), 1055–1073, 1990.

van den Heuvel, J. C., Driesenaar, M. L., and Lerou, R. J. L.: Fractal properties and denoising of lidar signals from cirrus clouds, J. Geo. Res., 105(D3), 3975–3982, 2000.

Voss, R. F. and Clarke, J.: 1/f noise in music: music from 1/f noise, J. Acoust. So., 63(1), 258-263, 1978.